bioRxiv preprint doi: https://doi.org/10.1101/2021.02.15.431207; this version posted February 16, 2021. The copyright holder for this preprint (which was not certified by peer review) is the author/funder. All rights reserved. No reuse allowed without permission.

Towards deciphering the Nt17 code: How the sequence and conformation of the first 17 amino acids in Huntingtin regulate the aggregation, cellular properties and neurotoxicity of mutant Httex1

Sophie Vieweg[1*], Anne-Laure Mahul-Mellier[1*], Francesco S. Ruggeri[2*], Nathan Riguet[1], Sean M. DeGuire[1], Anass Chiki[1], Urszula Cendrowska[2], Giovanni Dietler[2] and Hilal A. Lashuel[1†]

* These authors contributed equally to this work.

Corresponding author: Hilal A. Lashuel[†]

Affiliations:

[1] Laboratory of Molecular and Chemical Biology of Neurodegeneration, Brain Mind Institute, Ecole Polytechnique Fédérale de Lausanne (EPFL), 1015 Lausanne, Switzerland.

[2] Laboratory of the Physics of Living Matter, EPFL, 1015 Lausanne, Switzerland.

Note:

Current address of Francesco S. Ruggeri is Laboratory of Organic Chemistry and Laboratory of Physical Chemistry, Stippeneng 4, 6703 WE, Wageningen University, the Netherlands

Running title:

The Nt17 domain: a master switch of Htt aggregation and cellular properties

bioRxiv preprint doi: https://doi.org/10.1101/2021.02.15.431207; this version posted February 16, 2021. The copyright holder for this preprint (which was not certified by peer review) is the author/funder. All rights reserved. No reuse allowed without permission.

Abstract

The first 17 N-terminal amino acids (the Nt17 domain) flanking the polyQ tract of the Huntingtin protein (Htt) play an important role in modulating its aggregation, life cycle, membrane binding, and toxicity. Therefore, a better understanding of the molecular and structural determinants of the Nt17 code would likely provide important insights and help guide the development of future anti-aggregation and Htt lowering therapeutic strategies. Towards this goal, we sought to elucidate the role of the Nt17 sequence and helical conformation in regulating mutant Httex1 aggregation, morphology, uptake, and neuronal toxicity. To modulate the helical conformation of Nt17, we used a helix and membrane-binding disrupting mutation (M8P) strategy and site-specific introduction of post-translational modifications that are known to enhance (pT3) or disrupt (pS13, pS16, or pS13/pS16) the overall helicity of Nt17. Our *in vitro* studies show that the Nt17 and polyQ domains synergistically promote Httex1 aggregation, consistent with previous findings. However, we show that the Nt17 sequence, but not its helical conformation, is a key determinant of the morphology and growth of Httex1 fibrils. In cells, we show that the aggregation propensity and the toxic properties of *de novo* Httex1 were dependent on both the Nt17 sequence and its helical conformation and the synergistic effect of the Nt17 and polyQ domains. Finally, we demonstrate that the uptake of Httex1 into primary striatal neurons is strongly influenced by the helical propensity of Nt17. Phosphorylation (at T3 or S13/S16) or removal of the Nt17 domain increases the uptake and accumulation of Httex1 fibrils into the nucleus and induces neuronal cell death. Altogether our results demonstrate that the Nt17 domain serves as one of the key master regulators of Htt aggregation and toxicity and represents an attractive target for inhibiting Htt aggregate formation, inclusion formation, cell-to-cell propagation, and neuronal toxicity. These findings have significant implications for targeting the Nt17 domain to develop new disease-modifying therapies for the treatment of Huntington's disease.

bioRxiv preprint doi: https://doi.org/10.1101/2021.02.15.431207; this version posted February 16, 2021. The copyright holder for this preprint (which was not certified by peer review) is the author/funder. All rights reserved. No reuse allowed without permission.

Introduction

Huntington's Disease (HD) is an inherited brain disorder caused by a CAG repeat expansion within the first exon (Exon1) of the huntingtin gene (*htt)*[1,2]. Individuals with CAG repeats exceeding the pathogenic threshold of 36 CAG go on to develop HD, with the age of onset being inversely correlated with the number of the CAG repeats[3]. These HD mutations result in the production of a mutant Huntingtin (Htt) protein with an expanded polyglutamine (polyQ) domain (> 36Q repeats)[4,5]. Although the mechanisms by which these mutations cause HD continue to be intensively investigated and debated, the increased propensity of mutant Htt proteins to misfold, aggregate, and accumulate in intranuclear inclusions[6-10] suggests that polyQ-mediated Htt aggregation represents a central event in the pathogenesis of HD[11,12]. In addition to driving Htt aggregation, the expanded polyQ tracts have also been shown to modulate several aspects of Htt biochemical and cellular properties, including its subcellular localization[10], protein-protein interactions[13,14], proteolysis[15], and clearance[16-19].

To our knowledge, no report has suggested that the full-length Htt protein is capable of forming fibrils *in vitro* or established that nuclear Htt inclusions are made of fibrillar aggregates comprised of the full-length protein. By contrast, multiple N-terminal Htt fragments containing the polyQ domain have been identified in the neuronal intranuclear and cytoplasmic inclusions in several cellular and *in vivo* HD models[8,20-25] and post-mortem HD brains[11,26]. These observations have led to the hypothesis that the generation of N-terminal Htt fragments – by proteolysis[27-29] or alternative splicing[30,31] – and their aggregation is a key determinant of HD pathogenesis. The high aggregation propensity and toxicity of N-terminal Htt fragments, such as the Huntingtin Exon1 protein (Httex1), were initially attributed primarily to the presence of the polyQ domain[6,24,32-37]. However, increasing evidence from HD cellular and animals models suggests that the first 17 N-terminal amino acids (Nt17) play critical roles in regulating many aspects of Htt aggregation, life-cycles, subcellular localization, and toxicity in cells[38] and point to this Nt17 domain as one of the master regulators of Htt function in health and disease.

bioRxiv preprint doi: https://doi.org/10.1101/2021.02.15.431207; this version posted February 16, 2021. The copyright holder for this preprint (which was not certified by peer review) is the author/funder. All rights reserved. No reuse allowed without permission.

Therefore, deciphering the Nt17 code holds great potential for developing novel disease-modifying strategies based on Nt17-mediated modulation of Htt aggregation or degradation.

In the present study, we aimed to further refine our understanding of the sequence and structural determinants underlying the role of the sequence (post-translational modifications, PTMs) and conformation of the Nt17 domain in regulating the aggregation kinetics, fibril morphology, and cellular properties of Httex1, all in the context of tag-free Httex1 proteins with increasing polyQ-repeat lengths and in the same cellular/neuronal model systems. Motivated by recent studies[39-45] pointing to important roles of cell-to-cell propagation of mutant htt aggregates in the pathogenesis of HD[39-44], we also assessed the role of Nt17 and its helical conformation in the cellular uptake and the toxicity of Httex1 fibrils in primary striatal neurons. Our findings provide novel insights into the Nt17-dependent molecular and cellular determinants of Htt aggregation, inclusion formation, nuclear localization, and cell-to-cell propagation, with significant implications for targeting the Nt17 domain in the development of new disease-modifying therapies.

Results

The Nt17 domain accelerates the aggregation of Httex1 in a polyQ-dependent manner and strongly influences the final morphology of Httex1 fibrils

To investigate how the interplay between the Nt17 domain and the length of the polyQ repeat influences the aggregation properties of tag-free Httex1, we produced recombinant Httex1 proteins with different polyQ repeats ranging from 6Q to 42Q (6Q, 14Q, 22Q, 28Q, 36Q, 42Q) with or without Nt17 (ΔNt17-Httex1) (Figure S1). Next, we investigated the aggregation propensity of each protein by monitoring changes in the amount of remaining soluble protein over time using a sedimentation assay based on reverse-phase ultra-high-performance liquid chromatography (RP-UHPLC)[46]. As expected, the aggregation propensity of the Httex1 and ΔNt17-Httex1 proteins increased as a function of polyQ-length (Figure 1A). Notably, we observed a drastic increase in the aggregation propensity of Httex1 proteins with polyQ-lengths

bioRxiv preprint doi: https://doi.org/10.1101/2021.02.15.431207; this version posted February 16, 2021. The copyright holder for this preprint (which was not certified by peer review) is the author/funder. All rights reserved. No reuse allowed without permission.

between 22Q–28Q, below the clinical threshold of 36Q. Furthermore, the Nt17 domain significantly accelerated the aggregation of Httex1 compared to ΔNt17-exon1, consistent with previous in vitro aggregation studies based on synthetic polyQ or Exon1-like peptides[47-49] and Exon1 fusion proteins[50,51]. Using tag-free Httex1 proteins allowed us to investigate the aggregation process of native Httex1 sequences, thus avoiding potential influences/artefacts induced by the presence of tag peptides or proteins[52]. The aggregation-promoting Nt17-effect was observed in all Httex1 proteins, irrespective of the polyQ repeat lengths, but was especially pronounced for polyQ repeat lengths > 22Q, which we identified previously as the fibrillization threshold for mutant Httex1[53]. Interestingly, the aggregation of Httex1 36Q was complete within 24 h, seven times faster than for ΔNt17-Httex1 36Q, while the aggregation of Httex1-42Q was accelerated only by a factor of 3 compared to ΔNt17-Httex1 42Q. This indicates that the Nt17 effect diminishes with increasing polyQ-lengths, suggesting the polyQ and Nt17 domain synergistically modulate the aggregation propensity of Httex1.

Consistent with the sedimentation assays, the CD spectra after aggregation clearly showed a shift towards a cross-β sheet conformation for both the full-length and Nt17-truncated proteins (22Q to 42Q) (Figure S2). The time required for the conformational transition from disordered to cross-β sheet-rich structures for both the full-length and Nt17-truncated proteins (22Q to 42Q) during aggregation was inversely proportional to the polyQ repeat length (Figure S2).

Next, we investigated the role of the Nt17 domain in modulating the dimensions and morphology of Httex1 and ΔNt17-Httex1 (6Q–42Q) aggregates using high-resolution and phase-controlled atomic force microscopy (AFM)[54,55] in combination with single aggregate statistical analysis. We observed a direct correlation between the polyQ-length and the fibrillization propensity of Httex1 and ΔNt17-Httex1 proteins (Figures 1C and S3-S4), consistent with the sedimentation data in Figure 1A-B. The proteins with short polyQ domains of 6Q–22Q (Httex1 6Q, ΔNt17-Httex1 6Q/14Q) showed a low tendency (Httex1 14Q/22Q, ΔNt17-Httex1 22Q) to form fibrillar aggregates *in vitro* (Figures 1C and S3A, S4A). The fibrillization propensity of Httex1 and ΔNt17-Httex1 drastically increased when the polyQ-

bioRxiv preprint doi: https://doi.org/10.1101/2021.02.15.431207; this version posted February 16, 2021. The copyright holder for this preprint (which was not certified by peer review) is the author/funder. All rights reserved. No reuse allowed without permission.

length exceeded 22Q (Figures 1C and S3-S4). This is also reflected by the fact that these proteins exhibit the most dramatic change in secondary structure transition to a β-sheet conformation upon aggregation (Figure S2). Moreover, consistent with the sedimentation assay (Figure 1A-B), a time-dependent comparison of the aggregation tendency of these proteins showed that the presence of the Nt17 domain significantly enhanced the oligomerization and fibrillization of all the Httex1 proteins (14Q–42Q) compared to the corresponding ΔNt17-Httex1 proteins (Figure 1C).

To investigate how the Nt17 domain affects Httex1 aggregation, we performed a quantitative single aggregate statistical analysis of the morphology and cross-sectional dimensions of the fibrillar species observed in the high-resolution 3-D morphology maps acquired by AFM. We measured the cross-sectional height, convoluted width, and length of fibrils formed by Httex1 and ΔNt17-Httex1 proteins with increasing polyQ repeat lengths. For both Httex1 and ΔNt17-Httex1, we observed the formation of amyloid fibrils with a cross-sectional height between 5 and 7 nm. A time-dependent statistical analysis also revealed that the cross-sectional height of the fibrils as a function of incubation time and polyQ length, thus suggesting that both parameters are important to determine the formation of mature cross-β aggregates[54,56,57].
A different trend was observed for the length distributions of Httex1 and ΔNt17-Httex1.

Full-length Httex1 proteins with unexpanded polyQ repeats (22Q, 28Q) showed a broad fibril-length distribution ranging from 150 to 400 nm, whereas full-length proteins with expanded polyQ repeats (36Q, 42Q) formed fibrils with a significantly smaller length between 150 and 200 nm (Figure S3). This confirms previous findings from our group, showing that the fibril length of recombinant Httex1 proteins inversely correlates with the polyQ repeat length[53]. On the contrary, the fibril length of the ΔNt17-Httex1 protein increased significantly as a function of the length of the polyQ repeat. When the polyQ-length was increased from 22Q to 42Q, the ΔNt17-Httex1 fibril length increased from 200–300 nm to 200–600 nm, indicating a broadening of the length distribution as a function of polyQ repeat length (Figure S4). The fact that the

bioRxiv preprint doi: https://doi.org/10.1101/2021.02.15.431207; this version posted February 16, 2021. The copyright holder for this preprint (which was not certified by peer review) is the author/funder. All rights reserved. No reuse allowed without permission.

absence of the Nt17 domain negates the inverse correlation between fibril length and polyQ repeat length strongly suggests that the polyQ-Nt17 interactions play important roles in regulating Httex1 fibril growth.

High-resolution and -magnification AFM maps of Httex1 and ΔNt17-Httex1 fibrils (28Q, 36Q, 42Q) also revealed that removing Nt17 changes the surface properties of the fibrillar aggregates and induced significant lateral association and clumping of Httex1 fibrils (Figure 2). We investigated the extent of lateral fibril association by Httex1 and ΔNt17-Httex1 fibrils by TEM (Figure 2A) and measuring the width of the fibrils by AFM (convoluted width, Figure 2B-C)[55]. High-resolution AFM analysis showed a significantly broader width distribution for ΔNt17-Httex1 fibrils than Httex1 fibrils, irrespective of the polyQ repeat lengths (Figure 2C). Furthermore, the convoluted width of the fibrils for the ΔNt17-Httex1 proteins increased with increasing polyQ-length, whereas the convoluted width of the Httex1 fibrils converged around 20–25 nm, irrespective of the polyQ repeat length Httex1 (Figure 2C). Overall, this analysis demonstrates that the ΔNt17-Httex1 fibrils have a stronger tendency to associate at high polyQ repeat lengths than Httex1 fibrils laterally. Interestingly, trans-addition of the Nt17 peptide during the aggregation of ΔNt17-Httex1 fibrils did not alter the fibrillar interaction of ΔNt17-Httex1 (Figure S5), which showed significant lateral interaction.

Thus, the data indicate that intramolecular interactions between the Nt17 domain and the adjacent polyQ tract, rather than simple Nt17-mediated intermolecular interactions between Httex1 fibrils, are the primary driver of Httex1 lateral association. Taken together, this data suggests that the Nt17 domain influences fibril growth and surface properties of Httex1 fibrils which influence their intermolecular interactions and lateral association. The presence of the Nt17 at the fibrillar surface restricts their lateral interactions.

bioRxiv preprint doi: https://doi.org/10.1101/2021.02.15.431207; this version posted February 16, 2021. The copyright holder for this preprint (which was not certified by peer review) is the author/funder. All rights reserved. No reuse allowed without permission.

Disrupting the Nt17 helix (M8P mutation) slows the aggregation propensity of Httex1 *in vitro* but does not alter the morphology of the fibrils

Having established that the Nt17 domain modulates the aggregation kinetics and the fibril surface properties of Httex1 proteins, we next sought to determine whether these effects are mediated by amino acid sequence or the secondary structure properties of Nt17. Toward this goal, we introduced a methionine to proline mutation at position 8 within Nt17 (M8P)[58]. This mutation has been reported to disrupt the helical conformation of the Nt17 domain. Next, we compared the aggregation of this protein to that of Httex1 43Q and ΔNt17-Httex1 43Q. The purity of these three proteins was confirmed by sodium dodecyl sulfate-polyacrylamide gel electrophoresis (SDS-PAGE) (Figure S6A-B), mass spectrometry (Figure S6C) and both Western blotting (WB) (Figure 3A) and native gels (Figure 3B). Interestingly, in native gels, all three proteins appeared as two distinct bands, indicating that each protein exists in at least two different conformations. Despite the similar molecular weight and sequence of M8P-Httex1 43Q (12'471 Da) and Httex1 43Q (12'506 Da) (Figure S6C), M8P-Httex1 43Q migrates significantly higher, suggesting that the disruption of the Nt17 helical structure by the M8P mutation alters the conformation of soluble Httex1 (Figure 3B). Next, we assessed the aggregation kinetics of M8P-Httex1 43Q relative to Httex1 43Q and ΔNt17-Httex1 43Q. The introduction of the M8P mutation or deletion of the Nt17 domain resulted in significant retardation of Httex1 aggregation as discerned by the sedimentation assay (Figure 3C).

To determine the effect of the Nt17 domain on the surface properties of Httex1 fibrils, we prepared fibrils of Httex1, M8P-Httex1, and ΔNt17-Httex1 proteins (43Q) and examined their morphologies by TEM (Figures 3E and S6D). To ensure that morphological differences are not due to potential staining artifacts, we further performed cryo-electron microscopy (cryo-EM) on the aggregates formed by the three proteins (Figure 3D). The M8P mutation did not affect the final Httex1 fibril length as M8P-Httex1 formed fibrils with similar structure and dimensions as mutant Httex1 43Q (Figure 3D). In contrast, the removal of the Nt17 domain leads to a strong lateral association of the fibrillar aggregates with ribbon-like morphology (Figure 3D), similar to what we observed by AFM (Figure 2). Analysis of the same samples by negative-stain TEM

bioRxiv preprint doi: https://doi.org/10.1101/2021.02.15.431207; this version posted February 16, 2021. The copyright holder for this preprint (which was not certified by peer review) is the author/funder. All rights reserved. No reuse allowed without permission.

showed similar observations: Httex1 and M8P-Httex1 formed very smooth and regular fibrils, whereas the fibrils formed by Nt17-truncated Httex1 exhibited a higher tendency to undergo lateral association and form fibril bundles (Figure 3E). Quantification of the fibril lengths revealed average lengths of 200 nm Httex1 and M8P-Httex1 and 300 nm for the ΔNt17-Httex1 fibrils (Figure 3E). The quantification of fibril widths and lengths confirmed the similarities between M8P-Httex1 43Q and Httex1 43Q. Average lengths of 200 nm were determined for both Httex1 and M8P-Httex1 form fibrils with an average width of 5-10 nm compared to 15 nm for the ΔNt17-Httex1 fibrils as discerned by Cryo-EM (Figure 3D-E). Taken together, this data demonstrates that the Nt17 sequence, but not its helical structure, is the key determinant of the quaternary packing of Httex1 fibrils.

The helical conformation of the N17 domain is a key determinant of Httex1 aggregation in mammalian cells

Having demonstrated the significant influence of the Nt17 domain in regulating the aggregation kinetics and properties of Httex1 *in vitro*, we next sought to gain further insight on the role of the Nt17 domain in regulating Httex1 aggregation and inclusion formation in cells. Toward this goal, we used an HD mammalian cell (human embryonic kidney [HEK] cells) model system in which overexpression of Httex1 with polyQ > 39 repeats results in Htt inclusions formation[52,59,60]. Among these cells, ~85–90% showed cytoplasmic inclusions, while only ~10–15% of the cells had inclusions localized in their nucleus (Figure 4A-B)[52,59,60]. Therefore, we employed this model to investigate the effects of the sequence and helical conformation of the Nt17 domain on: 1) Httex1 aggregation and inclusions formation; 2) cytoplasmic vs. nuclear inclusion formation; and 3) the toxic properties of mutant Httex1. These effects were examined in the context of Httex1 carrying polyQ tracts of various lengths (16Q, 39Q, or 72Q), which also allowed us to investigate the effect of the Nt17 domain as a function of increasing polyQ-repeat length. Given that recent studies from our group demonstrated that the addition of a GFP tag to the Httex1 72Q protein dramatically influenced the biochemical composition and ultrastructural properties of Httex1 inclusions[52], we performed our studies using Httex1 or

bioRxiv preprint doi: https://doi.org/10.1101/2021.02.15.431207; this version posted February 16, 2021. The copyright holder for this preprint (which was not certified by peer review) is the author/funder. All rights reserved. No reuse allowed without permission.

ΔNt17-Httex1 constructs with different polyQ-repeat lengths (16Q, 39Q, and 72Q, Figure S7A) and fused or not to GFP. The use of Httex1-GFP fusion proteins allows us to compare our findings to published studies, most of which are based on the use of mutant Httex1-GFP/YFP proteins[61-70].

As expected, Httex1 16Q was exclusively expressed as diffuse proteins inside the cytosol, even 72 h post-transfection (Figure S7B) and inclusion formation was only observed in cells overexpressing Httex1 39Q or 72Q (24–48 h post-transfection) (Figure 4A-B). Most of these inclusions were formed in the cytosol in the vicinity of the nucleus, and ~10% were detected inside the nucleus (Figure 4C). As expected, the number of cells having inclusions was significantly higher for Httex1 72Q (~40%) than Httex1 39Q (16%) expressing cells (Figure 4A-B). On the other hand, we did not observe any impact of the length of the polyQ tract on the subcellular localization (Figure 4A, C) or the size (Figure 4A, D) of the Httex1 inclusions. Removal of the Nt17 domain (ΔNt17-Httex1 39Q or 72Q) did not significantly change the cellular distribution of Httex1 (Figure 4C), its ability to form aggregates (Figure 4A) or the mean size (Figure 4D) of the inclusions formed in HEK cells. However, quantitative confocal microscopy revealed that the number of cells showing inclusions was reduced by half when ΔNt17-Httex1 72Q was overexpressed compared to Httex1 72Q (Figure 4B). Such a difference was not observed with a shorter polyQ tract (39Q). This suggests that the polyQ and Nt17 domain synergistically modulate the aggregation propensity of Httex1 in cells, as observed *in vitro*.

Similarly, the introduction of the M8P mutation did not impact the subcellular localization (Figure 4C) or the size of the inclusions (Figure 4D) but resulted in a dramatic decrease (~76%) in the number of cells with inclusions (M8P-Httex1 72Q vs. Httex1 72Q) (Figure 4B). Interestingly, no significant differences in the level of inclusion formation was observed for the M8P constructs carrying 39Q or 72Q (Figure 4B). This finding underlies the interplay/synergy between the Nt17 and polyQ domain in regulating Htt aggregation. Interestingly, disruption of the helical conformation of mutant Httex1 in cells resulted in a significantly higher reduction in

bioRxiv preprint doi: https://doi.org/10.1101/2021.02.15.431207; this version posted February 16, 2021. The copyright holder for this preprint (which was not certified by peer review) is the author/funder. All rights reserved. No reuse allowed without permission.

inclusion formation compared to removal of the Nt17. This is in line with our *in vitro* aggregation results comparing M8P-Httex1 43Q and ΔNt17-Httex1 (Figure 3E). Altogether, our results demonstrate that both the sequence and the helical conformation of the Nt17 domain are major contributors to the aggregation enhancing properties of this domain.

The addition of GFP to the C-terminal part of Httex1 strongly influences its aggregation properties in cells

Interestingly, a similar number of cells showing inclusions was observed for the Httex1-GFP tagged constructs, regardless of the length of the polyQ tract (Httex1 39Q-GFP vs. Httex1 72Q-GFP). Moreover, in the presence of the GFP tag, the removal of the Nt17 domain no longer decreases the aggregation level in HEK cells (ΔNt17-Httex1-GFP 72Q vs. Httex1GFP 72Q) as observed for the tag-free constructs (ΔNt17-Httex1 72Q vs. Httex1 72Q), suggesting that the GFP masks the Nt17 effect (Figure 4B). Similarly, the reduction in the number of cells with inclusions was much less pronounced after overexpression of the M8P-Httex1-GFP 72Q than M8P-Httex1 tag-free (Figure 4B). This emphasizes our recent findings showing that the fusion of GFP proteins to Httex1 alters the structural and aggregation properties of the protein as well as its biological functions[52].

The conformation and sequence properties of the Nt17 domain are key determinants of the internalization and the subcellular localization of Httex1 fibrils in primary striatal neurons

An increasing body of evidence from cellular[39-41] and animal[42-44] HD models support the hypothesis that Htt pathology spreading plays an important role in disease onset and the progression of the HD pathology[45]. Based on the fact that the Nt17 domain associates with membranes and influences the subcellular localization of soluble Htt[58,71], we sought to investigate the role of the Nt17 domain in regulating the uptake of Httex1 and its potential contribution to the cell-to-cell propagation mechanisms. Toward this goal, fibrillar (Figure S6) and monomeric (Figures S8) WT Httex1 or mutant proteins (ΔNt17-Httex1 or M8P-Httex1)

bioRxiv preprint doi: https://doi.org/10.1101/2021.02.15.431207; this version posted February 16, 2021. The copyright holder for this preprint (which was not certified by peer review) is the author/funder. All rights reserved. No reuse allowed without permission.

were added to the extracellular media of striatal primary cultures and the internalization, subcellular localization, and toxicity of these proteins were evaluated for 6 days post-treatment.

Having demonstrated a drastic difference in fibrillar and surface properties between Httex1 and ΔNt17-Httex1 fibrils *in vitro* (Figure 1), we first sought to determine to what extent these differences influence the membrane association and the internalization of exogenous Httex1 43Q and ΔNt17-Httex1 43Q fibrils (Figure S9A) into a striatal primary culture (Figure 5). As shown in (Figure 5A), immunocytochemistry (ICC) combined with confocal microscopy showed that Httex1 fibrils mainly deposited overtime near the plasma membrane of cells that are positively identified as neurons by specific Microtubule-associated protein 2 (MAP2) neuronal staining; only a few aggregates were detected in the cytosol of these cells. To discriminate the fibrils internalized from those localized at the plasma membrane, we developed an unbiased semi-quantitative method based on confocal microscope imaging combined with an analytical pipeline that allowed distance map measurement (Figure S9C). This approach confirmed the accumulation of the Httex1 43Q fibrils near the neuronal plasma membrane (Figures 5B). However, as the resolution of confocal microscopy does not allow us to distinguish between the outer and the inner sides of the plasma membrane, we next used Correlative Light Electron Microscopy (CLEM) to visualize, at the ultrastructural level, the association of Httex1 43Q fibrils with the neuronal plasma membrane. CLEM imaging confirmed that most of Httex1 43Q fibrils were bound to the external side of the plasma membrane (Figures 5C, indicated by the black arrows and S10). Few Httex1 43Q fibrils were detected inside the endocytic vesicles (Figures 5C indicated by red asterisks and S10). In contrast, confocal imaging (Figure 5A) combined with the distance map measurements (Figure 5B) showed that the ΔNt17-Httex1 fibrils were readily internalized by the neurons (Figure 5A and B) and were rarely found associated with the plasma membrane. Interestingly, the Httex1-ΔNt17 43Q fibrils were detected primarily in the nucleus over the incubation period of 8 h to 6 days post-treatment (Figure 5D and E). The tight association of the Httex1 43Q fibrils with the plasma membrane could be attributed to the large number of Nt17 domains on the fibril surface and suggest that the Nt17 domain in Httex1

bioRxiv preprint doi: https://doi.org/10.1101/2021.02.15.431207; this version posted February 16, 2021. The copyright holder for this preprint (which was not certified by peer review) is the author/funder. All rights reserved. No reuse allowed without permission.

fibrils is highly dynamic and available for association with the membrane. This tight association with the plasma membrane impedes the internalization of Httex1 fibrils. Inside the neurons, Nt17 acts as a cytosolic retention signal[72,73] and prevents the translocation of the fibrils into the nuclear compartment. Removal of the Nt17 domain disrupts Httex1 fibrils' interactions with the membrane, thus facilitating their uptake and translocation to the nucleus. Altogether, our findings suggest a predominant role of the N17 domain in regulating Httex1 membrane binding, internalization, and subcellular localization.

Next, we investigated whether the helical conformation of the Nt17 domain is a key determinant of Nt17 interaction with biological membranes and can influence the internalization of Httex1 fibrils into neurons. To test this, we treated primary striatal neurons with fibrils derived from the M8P Httex1 mutant and assessed the extent of their internalization by ICC. Although the M8P derived fibrils exhibit similar morphology as WT Httex1 fibrils, the aggregated forms of the two proteins in cells exhibited a different cellular distribution. At the earliest time-points, M8P-Httex1 43Q fibrils were observed close to the plasma membrane, but in contrast to Httex1 43Q fibrils, these fibrils relocated over time inside the neurons in regions distal from the plasma membrane (Figure 5 A-B). The nuclear/cytoplasmic ratio measurements indicate that once internalized, the M8P-Httex1 43Q fibrils were equally distributed in the cytosol and nucleus (Figure 5 D-E).

Finally, we sought to determine whether Nt17 also regulates the internalization and the subcellular localization of monomeric WT (23Q) Httex1 species (Httex1, ΔNt17-Httex1, or M8P-Httex1) (Figure S11A). We choose to work with proteins with this polyQ repeat length (23Q) to maintain the proteins in a monomeric state and minimize potential aggregation over time, which was not possible with mutant Httex1 proteins (43Q) (Figure S8). In contrast to the fibrils (Figure 5), Httex1 23Q monomers were internalized efficiently (Figure S11B-C) and equally distributed between the cytosol and the nucleus (Figure S11D-E). However, as observed for the fibrils, the deletion of the Nt17 domain induced nuclear relocalization of

bioRxiv preprint doi: https://doi.org/10.1101/2021.02.15.431207; this version posted February 16, 2021. The copyright holder for this preprint (which was not certified by peer review) is the author/funder. All rights reserved. No reuse allowed without permission.

monomeric Httex1, while M8P proteins tend to be closer to the membrane area as observed for the fibrils (Figure S11C). Taken together, these results suggest that the uptake of the Httex1 monomers and fibrils into the striatal neurons and their subcellular localization is strongly dependent on both the sequence and helical conformation of the Nt17 domain.

Phosphorylation of T3, S13, and/or S16 residues promote the nuclear relocalization of Httex1 monomers

Several studies have shown that PTMs within the Nt17 domain could modulate the aggregation, subcellular localization, and toxicity of Httex1 via distinct mechanisms. Phosphorylation of Threonine 3 (pT3) stabilizes the Nt17 α-helical conformation and inhibits mutant Httex1 aggregation *in vitro*[46]. In contrast, phosphorylation of Ser13 and/or Ser16 (pS13/pS16) disrupts the helical conformation of Nt17 and inhibits mutant Httex1 aggregation *in vitro* and in cells[72,74,75]. While these findings suggest that the Nt17 helical propensity is not a good predictor of the aggregation of mutant Httex1, these PTMs provide a way to further assess the role of the Nt17 conformation in regulating the uptake and subcellular localization of Httex1. We have previously shown that phosphorylation at S13 and/or S16 favors the internalization of Httex1 pre-formed fibrils (PFFs) inside the neurons and their accumulation into the nucleus compared to their unmodified counterparts[75]. Next, we wanted to understand to what extent these PTMs could also alter the cellular properties of Httex1 monomers. Towards this goal, we generated monomeric preparations of Httex1-pT3 23Q, Httex1-pS13/pS16 23Q, and Httex1-pT3/pS13/pS16 23Q (Figure S9B), as previously described[75]. Figure 6A shows that the unmodified or phosphorylated Httex1 23Q monomers were all internalized inside the neurons. After 3 days of treatment, the phosphorylated Httex1 monomers (at pT3, pS13/pS16, or pT3/pS13/pS16) showed a significantly higher level in the nucleus than the unphosphorylated Httex1 23Q (Figure 6B-C). In contrast, unmodified Httex1 23Q seems to be equally distributed between the cytoplasm and nucleus compartment. Interestingly, both types of phosphorylation events, that enhance or disrupt Nt17 helical conformation, resulted in increased nuclear localization of Httex1, suggesting that the effect of

bioRxiv preprint doi: https://doi.org/10.1101/2021.02.15.431207; this version posted February 16, 2021. The copyright holder for this preprint (which was not certified by peer review) is the author/funder. All rights reserved. No reuse allowed without permission.

phosphorylation dominates the signaling events responsible for the nuclear translocation of Httex1.

The Nt17 domain and the polyQ length mediate Httex1 toxicity in cells

To determine whether the Nt17 domain also influences the toxic properties of Httex1, we first monitored the cell death level on HEK cells overexpressing Httex1 constructs (Httex1, ΔNt17-Httex1 or M8P-Httex1 with 16, 39 or 72Q) (+/-GFP) over time (Figures 7A-B and S12A-B). Initiation of apoptotic events was apparent only after 96 h in HEK overexpressing Httex1 72Q (+/-GFP), as indicated by Caspase 3 activation (Figure 7B) without loss of plasma membrane integrity, as determined by the Sytox blue assay (Figure 7A). The presence of the GFP tag did not influence the toxic properties of Httex1 72Q. Our findings show that the level of cell death correlated with the polyQ length, with Httex1 72Q (+/-GFP) being significantly toxic but not Httex1 16Q or 39Q (+/-GFP). Conversely, overexpression of ΔNt17-Httex1 72Q or M8P-Httex1 72Q constructs did not induce any toxicity in HEK cells, even 96 h after transfection. This suggests that removing the Nt17 domain or disrupting its helical structure is enough to prevent the cell death induced by Httex1 72Q in the HEK overexpression model. Besides, as shown in Figure 4B, the deletion of the Nt17 domain or the M8P mutation is sufficient to drastically reduce the number of cells with inclusions. This could also indicate that the cell death level correlates with the number of cells that contain inclusions.

To further investigate how the N17 domain influences Httex1 extracellular toxicity, we next evaluated cell death levels in the primary neuronal model. Httex1 monomeric (23Q) or fibrillar (23Q and 43Q) species were added exogenously to the neurons, and the toxicity was evaluated after 1, 3, or 6 days of treatment (Figures 7C-E and S12C-G). The overall toxicity in the primary neuronal culture, including cell loss of both neuronal and glial cells, was first quantified using the uptake of the vital dye Sytox Green as a marker for membrane disruption and toxicity. No toxicity was detected in neurons treated with 0.5 μM of monomeric Httex1 23Q, ΔN17-Httex1 23Q, M8P-Httex1 23Q (Figures 7C and S12C-D), or Httex1 23Q proteins

bioRxiv preprint doi: https://doi.org/10.1101/2021.02.15.431207; this version posted February 16, 2021. The copyright holder for this preprint (which was not certified by peer review) is the author/funder. All rights reserved. No reuse allowed without permission.

phosphorylated at the T3, S13, and/or S16 residues, even after 6 days of treatment (Figure 7D). The high propensity of the monomeric species to aggregate with increasing concentrations did not allow us to assess their toxicity at higher concentrations.

Next, we investigated the toxicity of WT or mutant Httex1 fibrils in primary neurons. No toxicity was observed after 1 day of treatment in neurons treated with the different types of pre-formed fibrils (PFFs) species (Figure S12E). However, starting at day 3, Httex1 PFFs eventually induced toxicity in a concentration-, time-, and a polyQ-dependent manner (Httex1 23Q vs. 43Q PFFs; (Figures 7F and S12D, F)). Intriguingly, although Httex1 and ΔNt17-httex1 fibrils exhibit major differences in membrane association, cellular uptake, and subcellular localization (Figure 5), a similar toxicity level was induced in the neurons treated with Httex1 43Q fibrils or ΔNt17-Httex1 43Q fibrils (Figure 7F). Conversely, Httex1 43Q M8P induced a lower level of toxicity in the striatal neurons than those treated with Httex1 43Q fibrils or ΔNt17-Httex1 43Q fibrils (Figure 7F). These results were confirmed using the TUNEL method (terminal deoxynucleotidyl transferase-mediated dUTP-biotin nick end labeling) as a complementary cell death method. Six days post-treatment, WT Httex1 43Q, ΔNt17-Httex1 43Q, and M8P-Httex1 43Q fibrils induced apoptosis in the neuronal population, positively stained for a specific neuronal marker (NeuN), with most of the cell death observed in neurons treated with ΔNt17-Httex1 43Q fibrils (Figure 7G and S12G). In contrast, M8P-Httex1 43Q fibrils were the least toxic to neurons (Figure 7G). Altogether, our data suggest that not only the polyQ length but also the Nt17 domain can modulate the toxicity of the Httex1 fibrils in primary striatal neurons.

Discussion

Even though the gene responsible of HD is known, we still do not understand the underlying mechanisms leading to neurodegeneration. Several lines of evidence support the hypothesis that the Nt17 domain of Htt plays important roles in regulating many of its physiological functions and pathological properties. However, previous studies aiming at elucidating the effect of the Nt17 domain on the Httex1 aggregation and fibril morphology were based on Httex1-like peptides or Httex1 fusion proteins, which do not contain the complete sequence of

bioRxiv preprint doi: https://doi.org/10.1101/2021.02.15.431207; this version posted February 16, 2021. The copyright holder for this preprint (which was not certified by peer review) is the author/funder. All rights reserved. No reuse allowed without permission.

Httex1 (e.g., Nt17 peptide) or are fused to a C-terminal S-tag (charged 15-mer peptide)[36,48,70] or to fluorescent proteins (e.g., GFP)[51,62,70,76,77]. We have previously demonstrated that the presence of such tags alters the ultrastructural and biochemical properties of Httex1 as well as its aggregation properties both *in vitro*[53] and in cells[52].

Therefore, in this study, we sought to decipher the Nt17 code by taking advantage of our tag-free Httex1 expression system. More specifically, we aimed to answer the following questions; 1) what is the effect of removing the Nt17 domain on the aggregation kinetics and fibril surface properties; and 2) what is the relative contribution of the sequence and helical conformation of the Nt17 domain to its effect on these properties Httex1 aggregation, membrane binding and internalization in cellular models of HD. In addition, we investigated for the first time, the role of the Nt17 sequence, PTMs and conformation in regulating the internalization and cell-to-cell propagation of monomeric and fibrillar forms of mutant Httex1.

The Nt17 and polyQ domains synergistically promote Httex1 aggregation.

Although the Nt17 domain has been shown to influence the aggregation of Httex1, the exact mechanisms by which it alters the structure and aggregation of Httex1 remain unknown. Our results show that the Nt17 and polyQ domains synergistically promote Httex1 aggregation *in vitro* (Figure 1). Similarly, in our overexpression-based cellular model, we have shown that the propensity of Httex1 to aggregate is enhanced with an increasing number of glutamine repeats in the polyQ domain. In contrast, disruption of the alpha-helical structure in the Nt17 domain decreases the propensity of Httex1 to form aggregates (Figure 4). Moreover, we discovered that at higher polyQ repeats above the pathogenic threshold, the Nt17 aggregation-enhancing effect (*in vitro*) becomes less evident (Figure 1), which is in agreement with findings from Williamson *et al.* showing that the polyQ domain (Q≥35) becomes the driving force of intermolecular association due to the enlarged interaction surface with increasing polyQ-length[60]. Therefore, we propose a modified model of the Httex1 aggregation pathway whereby the Nt17 domain influences the formation of amyloidogenic polyQ conformations, which

bioRxiv preprint doi: https://doi.org/10.1101/2021.02.15.431207; this version posted February 16, 2021. The copyright holder for this preprint (which was not certified by peer review) is the author/funder. All rights reserved. No reuse allowed without permission.

enhances intermolecular interactions and facilitates oligomerization, thus increasing the aggregation propensity of Httex1 (Figure 8).

Our TEM and AFM studies on Httex1 and ΔNt17-Httex1 aggregates showed that the length of fibrils formed by Httex1 inversely correlated with the polyQ content (Figures 1-2 and S3-S4), confirming previous results from our lab based on recombinant Httex1 proteins[53]. However, for ΔNt17-Httex1 proteins, the fibril length increased with increasing polyQ-length (Figures 1-2 and S3-S4), suggesting that the Nt17 domain mediates inter- and intramolecular interactions that regulate fibril growth and surface properties.

The Nt17 sequence, but not its helical conformation, is a key determinant of the surface properties and the morphology of Httex1 fibrils

We next investigated the relative contribution of the sequence and helical conformation of the Nt17 domain on the formation of Httex1 fibril and their morphology. Our structural study based on TEM, Cryo-TEM, and AFM analyses demonstrated the drastic morphological differences between Httex1 and ΔNt17-Httex1 aggregates (Figures 1-3 and S3-S4). Httex1 and ΔNt17-Httex1 fibrils had defined amyloid-like morphology similar to previously produced recombinant[53], semisynthetic[7,53,78], and synthetic Httex1[7,53,78,79]. However, ΔNt17-Httex1 formed fibrils, which have higher tendency to laterally associated into bundles. Conversely, introducing a helix-breaking mutation into the Nt17 domain (M8P) showed that the Nt17 effect on fibril structure is independent of the Nt17 conformation. In general, strong lateral interaction between fibrils leads to bundle formation and branching, which results in fibril bundles of variable width[77,80]. Indeed, amyloid-like Httex1 fibrils exhibited a narrower distribution of fibril widths from 15–25 nm, while the fibrils formed by ΔNt17-Httex1 fibrils showed a wider 20–40 nm distribution due to lateral association (Figures 1 and 2 and S3 and S4). Interestingly, the widths of ΔNt17-Httex1 fibrils diverged significantly with increasing polyQ-length, reflecting an increase in lateral interaction as a function of poly-Q (Figures 1 and 2 and S3 and S4). These findings suggest that the Nt17 domain restricts the intermolecular interactions between the polyQ domains and, thus, affects the surface properties of Httex1 during the aggregation

bioRxiv preprint doi: https://doi.org/10.1101/2021.02.15.431207; this version posted February 16, 2021. The copyright holder for this preprint (which was not certified by peer review) is the author/funder. All rights reserved. No reuse allowed without permission.

process. Notably, the smooth and uniform morphology of Httex1 fibrils has been shown in previous studies from our laboratory[7,53,81] and others using tag-free proteins[79]. However, our results are not in agreement with a previous study by Shen *et al.*, who report that removal of the Nt17 domain has the opposite effect, i.e., ΔNt17 promotes the formation of fibrils that exhibit a low tendency to laterally associated and form a "bundled architecture", which was characteristic of mutant Httex1 in their study[70]. Careful examination of their constructs reveals that they all contain a charged 15-mer peptide tag (S-tag: Lys-Glu-Thr-Ala-Ala-Ala-Lys-Phe-Glu-Arg-Gln-His-Met-Asp-Ser) at the C-terminus of Httex1, which we believe would strongly influence the aggregation properties of the mainly uncharged ΔNt17-Httex1 and Httex1 protein, thus possibly explaining the discrepancy between our findings and those of Shen *et al*[70]. These observations once again highlight the critical importance of using tag-free proteins to investigate the sequence and structural determinants of Httex1 aggregation and structure.

Based on our structural and cellular data, together with recent findings from other labs, we can propose a model for the role of the Nt17 domain in regulating the surface properties of Httex1 into fibrils and the internalization of Httex1 fibrils into primary rat striatal neurons. Amyloid proteins typically form cross-β-sheet-rich fibrils with a highly regular and smooth morphology, which originates from an in-register arrangement of β-sheets minimizing the possibility for lateral interaction[51,70,80,82]. We argue that the same packing mechanism forms Httex1 fibrils due to their uniform and smooth amyloid-like morphology, as previously demonstrated by our group[81] (Figures 1–3). Electron paramagnetic resonance (EPR) studies on Httex1 fibrils excluded the possibility of parallel in-register β-sheets in the fibril structure, while an in-register arrangement of anti-parallel β-sheets is in agreement with their data[83]. Indeed, our lab and others recently provided evidence for the existence of anti-parallel cross-β-sheets and β-hairpin in Httex1 fibrils[78,81]. Our data on the aggregation and structural properties of Httex1 and ΔNt17-Httex1 proteins suggest that the Nt17 domain directs the in-register arrangement of the β-sheets, and furthermore, its presence at the fibrillar surface limits the direct interaction of fibrillar cross-β the structure and the lateral association of fibrillar species (Figure 8, model).

bioRxiv preprint doi: https://doi.org/10.1101/2021.02.15.431207; this version posted February 16, 2021. The copyright holder for this preprint (which was not certified by peer review) is the author/funder. All rights reserved. No reuse allowed without permission.

The Nt17 domain likely regulates the quaternary packing through inter- and intramolecular interactions with the polyQ and the Nt17 domain[48,49,51,60]. On the contrary, the homopolymeric nature of the ∆Nt17-Httex1 proteins impedes a directional and strict in-register arrangement of β-sheets. The sequence-unspecific hydrogen bonds between the glutamine residues allow for the staggered arrangement of β-sheets, which enables the addition of β-sheets in parallel to the fibril axis (Figure 8C, model). This results in branching and the formation of and strongly-laterally associated fibrils, as observed for ∆Nt17-Httex1 (Figures 1–3). Moreover, our cellular studies comparing the membrane association and uptake of extracellularly added Httex1, ∆Nt17-Httex1 43Q and M8P-Httex1 43Q fibrils in primary rat striatal neurons (Figure 5) showed that the Nt17 domain must be part of the outer core of the Httex1 fibril, and at least partially solvent-exposed to be able to interact with the plasma membrane (Figure 8D, model). These findings provide strong evidence for a bottlebrush-like model of Httex1 fibrils, similar to the model proposed by Isas and Williamson *et al.*, with the exception that the Nt17 domain remains partially dynamic, which allows the Nt17 domain to mediate interactions between fibrils and biological membranes[60,84].

Taken together, our results demonstrate a critical role of the Nt17 domain in regulating the structure, morphology, and surface properties of Httex1 aggregates. Moreover, the conformational flexibility of the Nt17 domain might not only allow for Httex1 fibrils interactions with membranes but also regulate their interactions with other proteins.

The aggregation state of Httex1 and the helical conformation of Nt17 are key determinants of Httex1 membrane interaction and cellular uptake

Despite being an intracellular protein, recent evidence from neuronal grafts in HD patients[85], cellular[39-41] and animal[42-44] HD models suggest that Htt aggregates can be secreted by neurons and taken up by neighboring neurons leading to the speculation that this mechanism could contribute to the spreading of HD pathology in a prion-like manner[45,86], as recently reported for several proteins linked to other neurodegenerative diseases (e.g., α-synuclein in Parkinson's disease, Tau and amyloid-β in Alzheimer's disease, and TDP-43 in amyotrophic lateral

bioRxiv preprint doi: https://doi.org/10.1101/2021.02.15.431207; this version posted February 16, 2021. The copyright holder for this preprint (which was not certified by peer review) is the author/funder. All rights reserved. No reuse allowed without permission.

sclerosis [ALS])[87]. The membrane-binding capacity of the Nt17-domain depends on its amphipathic and α-helical structure. Therefore, mutations of PTMs that alter these properties are expected to play important roles in regulating Httex1 fibrils' interaction with the membrane and cellular uptake. Furthermore, it has been reported that the residues Leu4, Phe11, and Ser16 on HTT act as a NES (nuclear export signal) that is recognized by CRM1 and can export Htt from the nucleus following a Ran-GTP gradient[73]. Therefore, we assessed the uptake of Httex1 fibrils by striatal neurons and determined if the Nt17-mediated membrane binding plays a role in regulating Httex1 fibril internalization and subcellular localization. Our study demonstrated that Httex1 43Q fibrils accumulate near the plasma membrane area, whereas Httex1 43Q lacking the Nt17 domain was readily taken up by the striatal neurons and accumulate in the nuclear compartment over time (Figures 5 and S10). Furthermore, disruption of its helical conformation of Nt17 (M8P-Httex1 43Q fibrils) or modulation of the overall helicity of the protein through phosphorylation of T3 or S13 and/or S16 also results in a rapid uptake into striatal neurons. These findings suggest that the Nt17 helical conformation persists in the fibrillar state or that the Nt17 domain regains its helical structure upon interaction with the plasma membrane resulting in the sequestration of Httex1 fibrils at the membrane and impeding their uptake. Previous studies suggested that the Nt17 domain exhibits restricted conformational flexibility and is tightly bound to the polyQ fibril core, as evidence by their lack/reduced binding capacity to lipid membranes[37] and exhibit high stability against trypsin-mediated proteolysis with low cleavage rate at lysine residue[21]. In contrast, our studies confirmed the dynamic properties of Nt17 within Httex1 fibrils, as evidenced by their complete removal upon treatment of the fibrils with trypsin *in vitro* (Figure S13). These results suggest that the Nt17 domain is part of the outer surface of the Httex1 fibril, remains partially solvent-exposed, and can interact with the plasma membrane, thus providing strong evidence for the bottle-brush model of Httex1 fibrils proposed by Isas and Williamson *et al.*[60,84,88]. Moreover, the aggregation state of the protein seems to be important for protein-membrane interactions. Unlike the mutant Httex1 43Q fibrils, which exhibit strong binding to the plasma membrane, the unmodified monomeric Httex1 23Q proteins are taken up easily by neurons (Figures 5 and

bioRxiv preprint doi: https://doi.org/10.1101/2021.02.15.431207; this version posted February 16, 2021. The copyright holder for this preprint (which was not certified by peer review) is the author/funder. All rights reserved. No reuse allowed without permission.

S11). Altogether, our findings suggest that the uptake of fibrils into primary striatal neurons is strongly influenced by the helical propensity of the Nt17 domain and showed that Nt17 is exposed in the fibrillar state and is sufficiently dynamic to mediate fibril-membrane interactions and internalization.

Both the sequence and the helical conformation of Nt17 modulate the nuclear/cytoplasmic distribution of Httex1 species.

Previous studies have established an important role of the Nt17 domain, which can act as a nuclear export signal and regulator of the subcellular distribution of full-length Htt and N-terminal Htt fragments, including Httex1[58,70,73,89]. Our data are consistent with these studies and demonstrate that the Nt17 domain influences the nuclear/cytoplasmic distribution of Httex1: deletion of the Nt17 domain (Figures 5 and S11) led to increased translocation and accumulation of the Httex1 fibrils and monomers in the nucleus. Interestingly, disrupting the secondary structure of Nt17 did not show a similar increase in nuclear localization of exogenous Httex1 monomers and fibrils. Instead, Httex1-M8P 43Q fibrils and Httex1-M8P 23Q monomers were equally distributed between the cytosol and the nuclear compartment (Figures 5 and S11).

Mutant Htt is also known to undergo a nuclear localization in response to stress-mediated PTMs[74]. Therefore, we also assessed the impact of PTMs on Httex1 subcellular localization. Unlike previous studies that relied mainly on using phosphomimetic amino acids[73], we used site-specifically *bona fide* phosphorylated semisynthetic Httex1 proteins[75]. Monomeric Httex1 23Q phosphorylated on T3, S13/pS16, or T3/S13/S16 residues were readily taken up by striatal neurons and exhibited a greater tendency to accumulate more in the nucleus compared to unmodified Httex1 23Q monomers (Figure 6). Phosphorylation of either Ser13 or Ser16, induced by cellular stress, has already been shown to induce accumulation of Htt inside the nucleus. Interestingly, similar nuclear localization of Httex1 carrying phosphorylation on T3 and/or S13/S16 residues, despite the opposite effect of these modifications on the helicity of

bioRxiv preprint doi: https://doi.org/10.1101/2021.02.15.431207; this version posted February 16, 2021. The copyright holder for this preprint (which was not certified by peer review) is the author/funder. All rights reserved. No reuse allowed without permission.

Nt17; pT3 stabilizes the alpha-helical conformation of Nt17 while pS13 and/or pS16 disrupts it[75]. Whether the effect of phosphorylation on subcellular localization of Httex1 is mediated by its effect on the Nt17 conformation or charge state remains to be determined. Additional studies will be required to investigate further the role of the PTMs in modulating the role of Nt17 in controlling subcellular localization of Httex1. These observations could also suggest that the uptake and cellular properties of Httex1 are regulated by a complex interplay between the sequence (PTMs), the conformation of Nt17, and Httex1 interaction with other cellular factors or compartments.

The subcellular localization and the cell type influence the level of toxicity induced by Httex1 overexpression

Abnormal accumulation of neuronal Htt inclusions in brain regions affected in HD at late and more severe disease stages initially led to the direct relationship between protein misfolding, neuronal death, and disease progression[11,90]. However, several studies have shown that the correlation between the level of aggregation and neurotoxicity is imperfect, with some studies showing a strong correlation[11,90] while others do not[91,92]. Indeed, it has also been shown that the burden of inclusions bodies in human brain tissues does not predict the severity of neuropathology: in post-mortem tissues from HD patients, the highest level of cell death is observed in the striatum where only 1–4% of the striatal neurons contain Htt aggregates[91,92]. Conversely, a low level of neurodegeneration is observed in cortical neurons, which are heavily populated by Htt aggregates[91].

The causal relationship between the level of aggregates and the neuropathology also remains controversial. Expression of mutant N-terminal Htt fragments in neuronal cell models (Httex1, Htt1-480)[61,68,93,94] and transgenic mouse models (full-length YAC128 or short fragment of Htt with ~120Q)[94] of HD, showed that the frequency and size of cellular aggregates are inversely correlated with cell death. This suggests either 1) a protective role of Htt aggregates by reducing the level of the soluble toxic form of Htt[68,93,95], 2) neuroprotective effects of the

bioRxiv preprint doi: https://doi.org/10.1101/2021.02.15.431207; this version posted February 16, 2021. The copyright holder for this preprint (which was not certified by peer review) is the author/funder. All rights reserved. No reuse allowed without permission.

sequestration of toxic mutant Htt[61], or 3) the activation of neuronal cell death mechanisms (i.e., excitotoxicity) independent of the Htt aggregates formation[94]. Conversely, there is also opposing evidence from cellular models and animal models of HD suggesting that the formation and accumulation of intraneuronal mutant Htt positively correlate with the onset of behavioral phenotypes, the severity of the symptoms and the reduced survival in transgenic HD mice models (Htt1-117[96], Httex1[9,10,37,70,96,97], and the cellular neurotoxicity in mammalian cell lines[70]. In line with these findings, our overexpression-based model also shows polyQ length-dependent toxicity (Figure 7A-B). Removal of the Nt17 domain or disruption of its helical structure (M8P mutation) was sufficient to prevent the cell death induced by Httex1 72Q in the HEK overexpression model and reduce the number of cells with inclusions drastically. This could indicate that the cell death level correlates with the number of cells that contain inclusions or the number of inclusions formed in the cells or/and their subcellular localization. In contrast to our results, Shen et al.,[70] demonstrated that the overexpression of ΔN17-Httex1 induced toxicity at a similar level as the full-length Httex1 in striatal-derived neurons or neurons from cortical rat brain slices culture, although ΔN17-Httex1 led to a significant reduction of punctate structures in these cells. Besides, Atwal et al.[58] showed that overexpression of full-length Htt carrying the M8P mutation (Q138) greatly increased toxicity in STHdhQ7/Q7 cells. Finally, in transgenic mice models (i.e., BACHD-ΔN17 Htt mice[89] or in ΔN17 Htt zebrafish[98]), the deletion of the N17 domain accelerated the HD-like phenotype. The discrepancy between these studies and our Httex1 overexpression model in HEK cells may be due to the fact that in neurons, Httex1 lacking the Nt17 domain accumulates in the nucleus, whereas in HEK, it stayed mostly cytosolic. In line with this hypothesis, it has been recently shown that cytosolic inclusions (Httex1 200Q) and nuclear aggregates (Httex1 90Q) contribute – to various extents – to the onset and the progression of the disease in a transgenic HD mice model[99]. Thus, the difference in cellular localization but also the cell type (HEK vs. neurons) could influence the toxic response of the cells to the overexpression of ΔNt17-Httex1, with toxicity triggered only by the nuclear ΔNt17-Httex1 species.

bioRxiv preprint doi: https://doi.org/10.1101/2021.02.15.431207; this version posted February 16, 2021. The copyright holder for this preprint (which was not certified by peer review) is the author/funder. All rights reserved. No reuse allowed without permission.

Both the sequence and the helical conformation of the Nt17 domain influence the neurotoxic properties of Httex1

Next, we explored the toxicity of extracellular monomeric and fibrillar Httex1 species in primary striatal neurons and the relative contribution of the sequence and the helical conformation of the Nt17 to neuronal cell loss. As expected, the monomeric Httex1 species did not induce a measurable level of toxicity in primary striatal cells (Figure 7C and D). Our neuronal model also allowed us to assess the effect of PTMs (i.e., phosphorylation of Nt17) on the neuronal toxicity of extracellular species. In our hands, phosphorylation of the pT3, pS13 and/or pS16 residues did not render the Httex1 monomers toxic to primary striatal neurons (Figure 7D).

Conversely, Httex1 fibrils species exert toxicity in a polyQ length-dependent manner (Figure 7E). Our data show that the mutant Httex1 fibrils are anchored on the external side of the neuronal plasma membrane and are barely internalized into the neurons (Figure 5C). Interestingly, the accumulation of mutant Httex1 fibrils was concomitant with the loss of plasma membrane integrity (Figure 7E and F). In line with our findings, membrane damage caused by extracellular pathological aggregates has been previously suggested as a mechanism of pathogenesis in HD[100,101] but also in other prion-like diseases[102,103].

On the other hand, Httex1 43Q fibrils lacking the Nt17 domain were also highly toxic (Figure 7F), despite their rapid and efficient internalization and that they do not accumulate on the plasma membrane (Figure 5A, D, and E). Accumulation of nuclear ΔNt17-Httex1 aggregates has been previously shown to be highly toxic in several cellular and animal models[70,89,98].

Moreover, we showed that the disruption of the helical conformation of mutant Httex1 (M8P) fibrils resulted in a significant decrease in neuronal toxicity (Figure 7F and G). Our data confirmed that the neurotoxic response not only depends on the sequence of the Nt17 domain but also its conformation.

Interestingly, ΔNt17-Httex1 43Q fibrils exhibited higher toxicity compared to the M8P-Httex1 43Q fibrils. This difference in toxicity between M8P-Httex1 and ΔNt17-Httex1 fibrils does not

bioRxiv preprint doi: https://doi.org/10.1101/2021.02.15.431207; this version posted February 16, 2021. The copyright holder for this preprint (which was not certified by peer review) is the author/funder. All rights reserved. No reuse allowed without permission.

correlate with a difference in their capacity to be internalized: both proteins are readily taken up by primary striatal neurons (Figure 5). However, after their internalization, ΔNt17-Httex1 and M8P-Httex1 fibrils do not have the same cellular distribution with ΔNt17-Httex1 fibrils that significantly accumulate in the nucleus of the primary striatal neurons, while M8P-Httex1 fibrils are found both in the cytosol and the nucleus (Figure 5E). Our data suggest that the neurotoxic response is dependent on the subcellular localization of Httex1 species. This is in agreement with previous studies showing that nuclear targeting of Htt using nuclear localization signal (NLS)[104] or by the removal of Nt17 domain[58,70,89,105] increases toxicity. Nevertheless, we could not rule out that the high toxicity of ΔNt17-Httex1 fibrils could also be due to their distinct biophysical and structural properties. ΔNt17-Httex1 forms broad and fibrils characterized by lateral association, which could provide a surface for the sequestration of intracellular proteins (Figure 3).

Overall, our finding provides novel mechanistic insights into the role of not only the sequence but the conformational properties of the Nt17 domain in regulating the dynamics of the process of Httex1 fibrillization, the structure and morphology of Httex1 fibrils, and the cellular uptake and toxicity of mutant Httex1 monomers and fibrils. The use of the M8P mutation and site-specifically phosphorylated Httex1 proteins enabled us to dissect the relative contribution of the conformational and sequence properties of Nt17 and revealed the differential contribution of the two on 1) the morphology and surface properties of the fibrils; 2) the kinetics of growth of Httex1 fibrils; and 3) the uptake, the subcellular localization, and the toxicity of extracellular Httex1 species in neurons. Our results, combined with previous findings from our groups and others demonstrating the role of Nt17 in regulating Htt degradation[59,106,107], suggest that this domain serves as one of the key master regulators of Htt aggregation, subcellular localization of the pathological aggregates, and their toxicity. They further demonstrate that targeting Nt17 represents a viable strategy for developing disease-modifying therapies to treat HD. Future studies aimed at elucidating the role of Nt17 in the formation and stabilization of different aggregate along the Htt fibrillization and inclusion formation pathway and relative contribution

bioRxiv preprint doi: https://doi.org/10.1101/2021.02.15.431207; this version posted February 16, 2021. The copyright holder for this preprint (which was not certified by peer review) is the author/funder. All rights reserved. No reuse allowed without permission.

to the different proposed toxic mechanisms are likely to provide further insight that could guide the development of HD therapies.

Experimental procedures

Materials

Isopropyl-β-D-thiogalactopyranoside (IPTG) was ordered from Applichem (A1008,0025). Phenylmethane-sulfonyl fluoride (PMSF) was purchased from Axonlab (A0999.0005). CLAP protease inhibitor (1000x) was made of 2.5 mg/ml of Leupeptin, Chymostatin, Antipain and Pepstatin A from Applichem (A2183, A2144, A2129, A2205) in DMSO. The primary mouse anti-Huntingtin monoclonal antibody (MAB5492) were purchased from Millipore. Secondary goat anti-mouse labelled with Alexa680 was purchased from Invitrogen (A-21057). The PageRuler prestained protein ladder (26617), SeeBlue Plus2 pre-stained protein standard (LC5925) was purchased from Thermo Scientific was. Dulbecco's buffer substance (PBS) was purchased from Serva (47302.03). Microcon centrifugal filters with a MWCO of 100 kDa were obtained from Millipore (MRCF0R100) and PES syringe filter membranes with a pore size of 0.45 µm from Techno Plastic Products (TPP-99745). Formvar carbon film on 200-mesh copper grids (FCF200-Cu) and uranyl formate (16984-59-1) from Electron Microscopy Sciences were used for sample preparation for negative-stain Transmission Electron Microscopy (TEM). Ultra-sharp cantilevers (SSS-NCHR, curvature 2nm) were purchased from Park Systems (South Korea) and used for high-resolution Atomic Force Microscopy (AFM). The amyloid binding dye thioflavin S (ThS) was purchased from Sigma (T1892-25G).

Cloning, expression and purification

pTWIN1 vector (N6951S) and ER2566 *E.coli* (E6901S) competent cells were purchased from New England Biolabs. His6-Ssp-Httex1-QN cDNA was synthesized by GeneArt (Germany). Recombinant cDNA of His_6-Ssp-ΔNt17-Httex1-6Q/14Q/22Q/28Q/36Q/42Q containing a N-terminal cysteine (Q18C) for subsequent semisynthesis, His_6-Ssp-Httex1-23Q/43Q, His_6-Ssp-

bioRxiv preprint doi: https://doi.org/10.1101/2021.02.15.431207; this version posted February 16, 2021. The copyright holder for this preprint (which was not certified by peer review) is the author/funder. All rights reserved. No reuse allowed without permission.

ΔNt17-Httex1-43Q and His_6-Ssp-M8P-Httex1-43Q containing a M8P point mutation was synthesized and subcloned into the pTWIN1 vector (eBiolabs, N6951S) by GeneArt (Germany). Gene expression and protein purification were performed as previously described[7]. pCMV mammalian expression vector encoding for Httex1 16Q, Httex1 16Q-GFP, Httex1 39Q, Httex1 39Q-GFP, Httex1 72Q and Httex1 72Q-GFP were kindly provided by IRBM (Italy). ΔN17-Httex1 39Q, ΔN17-Httex1 39Q-GFP, ΔN17-Httex1 72Q, and ΔN17-Httex1 72Q-GFP were purchased from GeneArt (Germany). The substitution of the Methionine 8 for a Proline residue in the constructs provided by IRBM and listed above was engineered using the site-directed mutagenesis strategy. Huntingtin M8P primer Forward: 5'-GGA CTC GAA GGC CTT CGG CAG CTT TTC CAG GGT C-3' and Huntingtin M8P primer Reverse: 5'-GAC CCT GGA AAA GCT GCC GAA GGC CTT CGA GTC C-3' were purchased from Microsynth (Switzerland) and used PCR mutagenesis.

Semisynthesis of Httex1

Httex1 proteins for the structural analysis were obtained by native chemical ligation[79]. Therefore, the recombinant ΔNt17-Httex1 6Q/14Q/22Q/28Q/36Q/42Q (Q18C) proteins were ligated to a N-terminal acetylated synthetic Htt2-17 peptide (acATLEKLMKAFESLKSF), which carried a C-terminal N-acyl-benzimidazolinone (Nbz) moiety for thioester formation and was synthesized by CisBio. Desulfurization of the ligation products yielded the corresponding Httex1 proteins with a ligation scar (Q18A). Ligation and desulfurization were performed under conditions that inhibit Httex1 aggregation, as previously described[7,46,75].

Of note, we initially used semisynthetic proteins to conduct the aggregation studies. However, later on our group developed an efficient method for producing these proteins in Escherichia coli (E. coli). Therefore, the proteins used in the cellular studies were produced from (E. coli) and purified as described previously[75]. The phosphorylated proteins were produced using a chemoenzymatic approach recently developed by our group based kinase-mediated site-specific phosphorylation of Httex1 proteins[108].

bioRxiv preprint doi: https://doi.org/10.1101/2021.02.15.431207; this version posted February 16, 2021. The copyright holder for this preprint (which was not certified by peer review) is the author/funder. All rights reserved. No reuse allowed without permission.

Amino acid analysis

An aliquot of each protein (approximately 3 µg) was dried in an evacuated centrifuge and sent for amino acid analysis to the Functional Genomic Center Zurich (FGCZ) before aggregation to confirm the protein concentration determined by a RP-UPLC standard curve.

In vitro sedimentation assay

Lyophilized powder of semisynthetic Httex1, recombinant Httex1, ΔNt17-Httex1 and M8P-Httex1 proteins was prepared for the sedimentation assay as described previously[53,109]. In short, proteins were disaggregated by the addition of pure trifluoroacetic acid (TFA). After drying the TFA under a stream of dry nitrogen, proteins were dissolved in 10 mM PBS. Note that ΔNt17-Httex1 (6-42Q) proteins were dissolved in 10 mM PBS and 1 mM tris(2-carboxyethyl)phosphine (TCEP, Sigma-Aldrich) to keep the N-terminal cysteine reduced. After adjusting the pH to 7.2-7.4 all protein solutions were filtered through 100 kDa centrifugal filter units (MRCF0R100, Millipore). The protein concentrations were determined using a standard curve based on reversed-phase ultra-high performance liquid chromatography (RP-UHPLC) and confirmed by amino acid analysis (Functional Genomic Center Zurich). After transferring the proteins to 37°C, the decrease in soluble protein was determined over time by sedimentation. Therefore, aliquots of each protein sample were spun down at 20817xg at 4°C for 20 min and the soluble fraction was analysed by RP-UHPLC. 4 µL of the supernatant were injected into a C8 Waters Acquity UPLC BEH300 1.7 µm 300Å 2.1x150 mm column (method: 10-90%ACN in 2.75min, preheated to 40°C, flow rate of 0.6 ml/min) connected to an Acquity H-class UPLC system from Waters. Proteins eluted at 0.6 mL/min with a gradient from 10% to 90% acetonitrile (0.1% v/v TFA) over 2.75 min. The amount of soluble protein was calculated from the peak area using Empower Software from Waters. All data were normalized to t_{0h} and are represented as mean ± S.D. The elongation rates in Figure 1 were calculated as previously described[110]. During all aggregation experiments, the change in secondary structure was assessed by circular dichroism (CD), and the aggregate structure was imaged and quantified by atomic force microscopy (AFM) and transmission electron microscopy (TEM).

bioRxiv preprint doi: https://doi.org/10.1101/2021.02.15.431207; this version posted February 16, 2021. The copyright holder for this preprint (which was not certified by peer review) is the author/funder. All rights reserved. No reuse allowed without permission.

Thioflavin S (ThS) aggregation assay

For the ThS emission assay, 3 µM of Httex1-43Q, M8P-Httex1-43Q and ΔNt17-Httex1-43Q proteins were prepared as described for the sedimentation assay. However, to monitor the formation of amyloid fibrils, 10 µM of ThS were added to each protein sample before incubation of the proteins at 37°C. After addition of ThS, samples were transferred into the FLUOstar Omega plate reader (BMG LABTECH) and incubated at 37°C. The ThS emission was measured every 10 minutes using a filter for wavelengths of 440-480 nm.

Secondary Structure Analysis by CD

100 µl of each protein solution was transferred into a 1 mm quartz cuvette for analysis of the secondary structure by a J-815 CD spectrometer from Jasco. Acquisition of the molar ellipticity was performed at 25°C from 195 nm – 250 nm, and data points were acquired continuously every 0.2 nm at a speed of 50 nm/min with a digital integration time of 2s and a bandwidth of 1.0 nm. For each sample, 5 spectra were averaged. After background subtraction, the obtained spectra were smoothened using a binomial filter with a convolution width of 99 data points.

EM imaging and quantification

To image the structure and morphology of formed oligomers and fibrils by transmission electron microscopy (TEM), protein *s*amples were deposited on formvar/carbon-coated 200-mesh copper grids (FCF200-Cu, Electron Microscopy Sciences) for 1 min at RT. Then the grids were washed and stained with a 0.75% w/v uranyl formate (Electron Microscopy Sciences) solution in water. Grids were imaged using a Tecnai Spirit BioTWIN microscope at 80 kV (LaB6 gun, 0.34nm line resolution) equipped with a 4k x 4k Eagle CCD camera with high sensitivity scintillator from FEI. Fibril lengths and widths were quantified using ImageJ software[111]. In parallel, samples were prepared for atomic force microscopy (AFM) to measure the fibril height, length and width. High-resolution images (1024x1024 pixels) were collected

bioRxiv preprint doi: https://doi.org/10.1101/2021.02.15.431207; this version posted February 16, 2021. The copyright holder for this preprint (which was not certified by peer review) is the author/funder. All rights reserved. No reuse allowed without permission.

using an NX10 Atomic Force Microscope (Park Systems, South Korea) in ambient conditions and in non-contact Amplitude Modulation (NC-AM). We imaged square areas of 2x2 μm2 and 4x4 μm2. We performed all the measurements using ultra-sharp cantilevers (SSS-NCHR, Park Systems, South Korea) with a resonance frequency of 330 kHz and a typical radius of curvature of 2 nm. In order to compare the height of different samples consistently, we established standardized experimental scanning conditions, and we maintained a regime of phase change in the order of ≈Δ20°. Raw images were flattened with the XEI software (Park System, South Korea). During the process of flattening of the images, the aggregates were masked from the calculation to avoid modification and underestimation of their height. We compared the structural difference between different samples through accurate control of the sample-tip interaction while scanning the probe through the sample.

Cryo-electron microscopy

Lyophilized powder of recombinant Httex1, ΔNt17-Httex1 and M8P-Httex1 proteins (43Q) were disaggregated by the addition of pure TFA. After acid evaporation under a stream of dry nitrogen, proteins were dissolved in 10 mM PBS to obtain a protein concentration of 300 μM. The pH was adjusted to pH 7.2-7.4, and samples were kept at 30°C for 3 days before imaging. The fibrils were prepared for cryo-EM, and imaging of the samples was performed as described previously described[112,113]. In short, an EM grid (Agar scientific, UK) with holey carbon film was held with tweezers. 4-5 μL of sample solution was applied on the grid and tweezers were mounted in an automatic plunge freezing apparatus (Vitrobot, FEI, The Netherlands) to control humidity and temperature. After blotting, the grid was immersed in a small metal container with liquid ethane that is cooled from outside by liquid nitrogen. The speed of cooling is such that ice crystals do not have time to form. The observation was made at -170°C in a Tecnai F 20 microscope (FEI, Eindhoven, The Netherlands) operating at 200 kV and equipped with a cryo-specimen holder Gatan 626 (Warrendale, PA). Digital images were recorded with an Eagle (FEI) camera 4098 X 4098 pixels. Magnification between 20’000-30’000X, using a defocus range of 2-3 μm.

bioRxiv preprint doi: https://doi.org/10.1101/2021.02.15.431207; this version posted February 16, 2021. The copyright holder for this preprint (which was not certified by peer review) is the author/funder. All rights reserved. No reuse allowed without permission.

AFM

The samples were prepared for atomic force microscopy (AFM) to measure the fibrillar cross-sectional diameter (height) and length, as well as the width of associated fibrils. High-resolution images (1024x1024 and 2048x2048 pixels) were collected using an NX10 Atomic Force Microscope (Park Systems, South Korea) in ambient conditions and in non-contact Amplitude Modulation (NC-AM)[55]. We imaged square areas of 2x2 µm2 and 4x4 µm2. We performed all the measurements using ultra-sharp cantilevers (SSS-NCHR, Park Systems, South Korea) with the resonance frequency of 330 kHz and a typical radius of curvature of 2 nm. In order to compare the height of different samples consistently, we established standardized experimental scanning conditions and we maintained a regime of phase change in the order of ≈Δ20°[55,81]. Raw images were flattened with the XEI software (Park System, South Korea) and statistical analysis was performed by SPIP (Image Metrology, Denmark).

Fibril preparation for cellular studies

Lyophilized powder of recombinant Httex1 23Q, Httex1 43Q, ΔNt17-Httex1 42/43Q and M8P-Httex1 43Q was disaggregated with formic acid. After evaporation of the acid, proteins were dissolved in 50 mM Tris, 150 mM NaCl, pH 7.4 buffer to obtain a final concentration of 200 µM (2.5 mg/mL for expanded and 2 mg/mL for unexpanded Httex1, 2.1 mg/mL for expanded and 1.6 mg/mL for unexpanded ΔNt17-Httex1 proteins). Solutions were incubated at 37°C and fibril formation was monitored by Coomassie gel and CD. Fibrils were diluted 1/10 in water before analysis. For SDS-PAGE and Coomassie staining, each sample was mixed with 4x Laemmli buffer, and 15 ul of each mixture were loaded on a 15% SDS gel without prior boiling of the sample. When complete aggregation was reached, the fibrils were sonicated (twice, 40% amplitude, 2x 5s) and imaged by TEM. To ensure that cells are treated with similar amounts of fibrils, the concentration of each aliquot was compared using Ponceau staining. Therefore, 2 µl of each sample were spotted on a nitrocellulose membrane and dried for 60s. The membrane was stained with Ponceau and destained with water. The intensity of the spots was

bioRxiv preprint doi: https://doi.org/10.1101/2021.02.15.431207; this version posted February 16, 2021. The copyright holder for this preprint (which was not certified by peer review) is the author/funder. All rights reserved. No reuse allowed without permission.

analyzed by ImageJ and normalized to the intensity of recombinant Httex1-23Q or -43Q, respectively.

SDS-PAGE, Coomassie staining and WB analysis

Samples for SDS-PAGE (sodium dodecyl sulphate-polyacrylamide gel electrophoresis) were mixed with 4x Laemmli and loaded onto 15% polyacrylamide gels[114]. Electrophoresis was performed at 180 V for 1h. Proteins in the gels were either directly stained with a Coomassie R-450 solution and destained in water or transferred on a nitrocellulose membrane (0.2 µm, Amersham) using the semidry transfer systems from BioRad using 200 mA at 25V for 1h. Nitrocellulose membranes were incubated in Odyssey blocking solution from Licor (30 min at RT) and later blotted with primary mouse anti-Htt MAB5492 from Millipore (12-16 h at 4°C). Membranes were washed 3 times in PBS-Tween 1% and then incubated with the secondary Alexa680-conjugated goat anti-mouse (Licor) for 45 min at RT. After 3 washes in PBS-Tween 1%, fluorescence intensity from the proteins of interest were detected with the Odyssey Infrared Imager system from Licor.

Native gel and WB analysis

Protein samples for native gels were mixed with 5x native sample buffer (Laemmli buffer without SDS or reducing agent) and without boiling 15 µl were loaded on a Tris-based native gel containing 7.5% acrylamide and no SDS. Electrophoresis was performed at 180 V for 2-2.5h. Proteins were transferred to a nitrocellulose membrane by semidry transfer for 1h at constant 200 mA and 25V. The nitrocellulose membrane was blocked and treated with antibodies, as described above.

Primary culture of rat striatal neurons

All animal procedures were approved by the Swiss Federal Veterinary Office (authorization number VD 2137). Primary rat striatal neurons culture, prepared from P0 pups from rat (OFA SD, Charles River), were adapted for the protocol previously described[115]. Briefly, the cerebral

bioRxiv preprint doi: https://doi.org/10.1101/2021.02.15.431207; this version posted February 16, 2021. The copyright holder for this preprint (which was not certified by peer review) is the author/funder. All rights reserved. No reuse allowed without permission.

striatum was isolated stereoscopically and dissociated by trituration in a medium containing papain (20U/mL, Sigma-Aldrich, Switzerland). Rat striatal neurons were cultured in Neurobasal medium containing B27 supplement, L-glutamine and penicillin/streptomycin (Life Technologies, Switzerland). The neurons were seeded in 96 wells plates or onto coverslips (CS) (VWR, Switzerland) previously coated with poly-L-lysine 0.1% w/v in water (Sigma-Aldrich, Switzerland) at a density of 150,000 cells/mL. After 3 days, the cells were treated with cytosine β-*D*-arabinofuranoside (Sigma-Aldrich, Switzerland) to a final concentration of 2.3 µM to inhibit glial cell division.

After 14 days in culture (2 weeks old), the primary striatal neurons were treated with Tris buffer (negative control), extracellular pre-formed fibrils (PFFs, 0.5 µM) of Httex1 43Q, Httex1-ΔNt17 43Q and Httex1-M8P 43Q or with 0.5 µM of monomeric Httex1-23Q, Httex1-ΔNt17 23Q and Httex1-M8P 23Q or with 0.5 µM monomeric Httex1 carrying phosphorylation on the residue threonine residue (Httex1-pT3) or on the serine residues at the position 13 or 16 (Httex1-pS13/pS16) or at the 3 positions (Httex1-pT3/pS13/pS16). Httex1-pT3, Httex1-pS13/pS16 and Httex1-pT3/pS13/pS16 were prepared as previously described[75]. 1 day (D1), 3 days (D3 or 6 days (D6) after the addition of the recombinant extracellular proteins, striatal neurons were washed 3 times with PBS and then fixed in 4% PFA (paraformaldehyde) for 10 min at RT before the immunocytochemistry procedure.

HEK cell culture and plasmid transfection

HEK 293 cells were maintained in Dulbecco's modified Eagle's medium DMEM (Life Technologies, Switzerland) containing 10% foetal bovine serum (FBS, Life Technologies, Switzerland), 10 µg/ml streptomycin and penicillin (Life Technologies, Switzerland) in a humidified incubator, 5% CO2, 37°C. Cells were plated at a density of 50 000 cells/ml in 24 well plates (BD, Switzerland), in order to have cells at 70% confluence the day of the transfection. HEK 293 were transfected using the standard calcium phosphate procedure[116]. Briefly, 2µg of the mammalian plasmid coding for Httex1 (16Q, 39Q or 72Q, +/- GFP), ΔNt17-Httex1 (16Q, 39Q or 72Q, +/- GFP) or M8P-Httex1 (16Q, 39Q or 72Q, +/- GFP) was diluted in

bioRxiv preprint doi: https://doi.org/10.1101/2021.02.15.431207; this version posted February 16, 2021. The copyright holder for this preprint (which was not certified by peer review) is the author/funder. All rights reserved. No reuse allowed without permission.

30µl H2O, and 30µl of 0.5M CaCl2 before dropwise addition of 60µl of 2xHBS, pH 7.2 (50mM HEPES, pH 7.05; 10mM KCL; 12mM dextrose; 280mM NaCl; 1.5mM Na2PO4, pH 7.2 dissolved in H2O) under mild vortexing condition. 48 hours after transfection, HEK 293 cells were washed twice with PBS and fixed in 4% paraformaldehyde (PFA, Sigma-Aldrich, Switzerland) in PBS for 20 min at 4 °C before the immunocytochemistry procedure.

Immunocytochemistry (ICC)

After a blocking step with 3% BSA diluted in 0.1% Triton X-100 PBS (PBST) for 30 min at room temperature (RT), HEK 293 cells or the primary striatal neurons were incubated with the primary antibody anti-htt (MAB5492, RRID:AB_347723, Millipore, Switzerland) at a dilution of 1/500 in PBST for 2 h at RT. Striatal neurons were co-stained with the primary chicken antibody anti-MAP2 (neuronal marker, RRID:AB_2138147, Abcam, United Kindom) at 1/2000. Cells were then rinsed five times in PBST and then incubated for 1 hour at RT with the secondary donkey anti-mouse Alexa647 antibody (RRID:AB_162542, Life Technologies, Switzerland) at a dilution of 1/800, and/or with the donkey secondary anti-chicken Alexa488 (RRID:AB_2340375, Jackson Immunoresearch, United Kingdom) and DAPI (4′,6-Diamidine-2′-phenylindole dihydrochloride for nuclear staining, Sigma-Aldrich, Switzerland) at a dilution of 1/2000, all prepared in PBST. To visualize the edge of the HEK 293 cells, Phalloidine Atto594 (specific against F-actin) was used at a dilution of 1/50 for 1 hour at RT (Sigma-Aldrich, Switzerland). Cells were then washed five times in PBST. A last wash was performed in pure water, before mounting the coverslips in polyvinyl alcohol (PVA) mounting medium with DABCO (Sigma-Aldrich, Switzerland). Cells were examined with confocal laser-scanning microscope (LSM 700, Zeiss, Germany, RRID:SCR_017377) with a 40xobjective and analyzed using Zen software (Zeiss, Germany, RRID:SCR_013672).

Measurement of the subcellular localization of Httex1 constructs in primary striatal neurons

bioRxiv preprint doi: https://doi.org/10.1101/2021.02.15.431207; this version posted February 16, 2021. The copyright holder for this preprint (which was not certified by peer review) is the author/funder. All rights reserved. No reuse allowed without permission.

As all the Httex1 species do not run equally in a SDS-PAGE gel (e.g: Httex1 fibrils do not enter into SDS-PAGE gel and stay mainly in the wells of the stacking part; ΔNt17-Httex1 constructs have a low charge state and low SDS-binding capacity and are characterized by aberrant mobility in SDS-Gels), we have developed an unbiased semi-quantitative method based on confocal microscope imaging combined with an analytical pipeline using Image J and CellProfiler 2.2.0 software to quantitatively assessed the cellular properties of Httex1 in our neuronal model (Figure S8). For each independent experiment, a minimum of 5 neurons per condition was imaged. Each independent experiment was done in triplicate resulting in the acquisition of 15 neurons in total per condition tested. For each neuron, a series of images was collected (z-stack, 13 slices with a thickness of 0.2 µM) from the top to the bottom of the nucleus area. From the acquisition of the neuronal Z-stack, the neuronal slice was selected via Image J with criteria to avoid selecting the neurites. Neurites extensions were avoided during the imaging process as their length can greatly vary between neurons, which could lead to unspecific variation in our quantification. Then from the selected image, the segmentation of the nucleus was performed from the DAPI signal and membrane from the MAP2 staining using CellProfiler software. Cytoplasm and nuclear masks were automatically created and used to measure mean intensity fluorescence of Httex1 species, detected with a specific Htt antibody, in the different compartments. The BioP (EPFL, Switzerland, Dr Romain Guiet) developed a distance maps script to more accurately quantify the detected Httex1 particles distance from the plasma membrane. The generated regions of interest from CellProfiler (nucleus and cytoplasm) were used to create a distance map from the plasma membrane inside and outside of the neurons. Httex1 species were detected as particles via intensity thresholding and plotted according to their distance to the plasma membrane either internalized or on the outside of the cell. The resolution under the confocal microscope did not allow for exact localization of the detected Httex1 particles at the plasma membrane (10nm) and was considered as a “membrane area”.

Correlative Light Electron Microscopy

bioRxiv preprint doi: https://doi.org/10.1101/2021.02.15.431207; this version posted February 16, 2021. The copyright holder for this preprint (which was not certified by peer review) is the author/funder. All rights reserved. No reuse allowed without permission.

Striatal primary neurons were seeded on 35 mm dishes with alpha-numeric searching grids etched to the bottom glass (MatTek Corporation, Ashland, MA, USA) coated with poly-L-lysine (Life Technologies, Switzerland) and treated with Tris buffer (negative control) or 0.5 µM of extracellular of Httex1-43Q PFFs. After 3 days, striatal neurons were fixed for 2 h with 1% glutaraldehyde and 2.0% PFA in 0.1 M phosphate buffer (PB) at pH 7.4. Then, ICC was performed as described in the corresponding section of the Material and method. The neurons positively stained for Httex1 were selected by fluorescence confocal microscopy (LSM700, Carl Zeiss Microscopy), and its exact position was recorded using the alpha-numeric grid etched on the dish bottom. The neurons were then fixed, dehydrated, and embedded with Durcupan (Electron Microscopy Sciences, Hatfield, PA, USA) as previously described[52,117,118]. The ultrathin sections (50–60 nm) cut serially and collected onto 2 mm single-slot copper grids coated with formvar plastic support film were finally contrasted with uranyl acetate and lead citrate before being imaged with a transmission electron microscope (Tecnai Spirit EM, FEI, The Netherlands) operating at 80 kV acceleration voltage and equipped with a digital camera (FEI Eagle, FEI)[52,117,118].

Quantification of cell death in striatal primary neurons and HEK 293 cells

Quantification of cell death by dye exclusion method in rat striatal primary neurons and HEK 293 cells

Rat striatal primary neurons were plated in 96 wells plate coated with poly-L-lysine (Life Technologies, Switzerland) and treated with 0.5, 1 and 2µM of extracellular Httex1-23Q/43Q, ΔN17-Httex1-23Q/43Q fibrils or M8P-Httex1-23Q/43Q fibrils for one day (D1), 3 days (D3) and 6 days (D6). HEK cells transfected with the mammalian plasmid coding for Httex1 (16Q, 39Q or 72Q, +/- GFP), ΔNt17-Httex1 (16Q, 39Q or 72Q, +/- GFP) or M8P-Httex1 (16Q, 39Q or 72Q, +/- GFP) for 72 hours and 96 hours.

The vital dye exclusion method was used to quantified cells death in neurons with Sytox Green (SG) and in HEK 293 cells with Sytox Blue (SB) for the HEK 293 cells (Life Technologies, Switzerland), a membrane impermeant dye which enters only in cells with damaged plasma

bioRxiv preprint doi: https://doi.org/10.1101/2021.02.15.431207; this version posted February 16, 2021. The copyright holder for this preprint (which was not certified by peer review) is the author/funder. All rights reserved. No reuse allowed without permission.

membranes as previously described[103,117,118]. Briefly, after 3 washes with PBS, the cells were incubated with SG (neurons) or SB (HEK 293 cells) at a final concentration of 330 nM. After 15 minutes of incubation, cells were washed twice with PBS and fluorescence was quantified using by using Tecan infinite M200 Pro plate reader (Tecan, Switzerland) with respective excitation and emission wavelength of 487 nm and 519 nm.

Quantification of active caspases 3 in HEK293 cells

As described previously[103,118], we used caspaTag fluorescein caspase 3 activity kit (ImmunoChemistry Technologies, MN, USA), which allows the detection of active effector caspase (caspase 3) in living cells. These kits used the specific fluorochrome peptide inhibitor (FAM-DEVD-fmk) of the caspase 3 (FLICA). This probes passively enter the cells and bind irreversibly to the active caspases. HEK293 were washed twice with PBS and incubated for 30 min at 37 °C with FAM-DEVD-FMK in accordance with the supplier's instructions. Tecan infinite M200 Pro plate reader (Tecan, Switzerland) was used to quantify the fluorescein intensity with respective excitation and emission wavelength of 487 nm and 519 nm.

Terminal deoxynucleotidyl transferase-mediated dUTP-biotin nick end labeling method (TUNEL) in primary striatal neurons

DNA fragmentation was detected using the terminal deoxynucleotidyl transferase-mediated dUTP-biotin nick end labeling (TUNEL) method described by Gavrieli et al.[119]. Rat striatal primary neurons were seeded on coverslips coated with poly-L-lysine (Life Technologies, Switzerland) and treated with 0.5, 1 and 2 µM of extracellular Httex1-23Q/43Q, ΔN17-Httex1-23Q/43Q fibrils or M8P-Httex1-23Q/43Q fibrils. After six days of treatment, rat striatal neurons were washed three times with PBS before being fixed in 4% PFA for 15 min at 4°C. Cells were then permeabilized with 0.1% Triton X-100 in 0.1% citrate buffer, pH 6.0. Neurons were washed in PBS buffer before being incubated with the terminal deoxynucleotide transferase (In Situ Cell Death Detection kit) (Roche, Switzerland) for 1 h at 37°C in a solution containing TMR red dUTP. The neurons were then specifically stained for NeuN (RRID:AB_2298772,

bioRxiv preprint doi: https://doi.org/10.1101/2021.02.15.431207; this version posted February 16, 2021. The copyright holder for this preprint (which was not certified by peer review) is the author/funder. All rights reserved. No reuse allowed without permission.

Millipore, Switzerland), a nuclear neuronal marker (see ICC section). After 5 washes with PBS, neurons were mounted in in polyvinyl alcohol (PVA) mounting medium with the anti-fading DABCO reagent (Sigma-Aldrich, Switzerland). The neurons plated on CS were then examined with a microscope (Axioplan, Carl Zeiss Microscopy) with a 20× objective and analyzed using Image J (U.S. National Institutes of Health, Bethesda, Maryland, USA)[111] as described before[103,118].

Statistical analysis

All the experiments were independently repeated three times. Analysis of the set of data generated by Cell profiler software was performed using Excel and Graphpad Prism software (RRID:SCR_002798). Statistical analysis was performed using Anova followed by a Tukey-HSD test. The data were regarded as statistically significant at $p<0.05$.

Acknowledgments

This work was supported by funding from EPFL, the Cure Huntington's Disease Initiative (CHDI) foundation and the Swiss National Science Foundation (SFN). We are grateful to the Biological Electron Microscopy facility (EPFL), and the Bio-imaging Core Facility (EPFL) for their technical support and helpful discussions. We thank in particular Dr. Romain Guiet for his help in developing the distance map script and Mary Croisier for the acquisition of the CLEM images. We also deeply thank Sergey Nazarov for his inputs and help in drawing the final model in Figure 8.

Author contributions

H.A.L conceived and supervised the study. H.A.L, S.V, A.L.M.M, F.S.R and N.R wrote the paper. S.V and F.S.R. designed, performed and analysed the experiments shown in Figures 1-3 and Figures S1-S2, S5-S7 and S11. A.L.M.M designed, performed and analyzed the experiments shown in Figures 4-7 and Figures S8, S10-S11 and S12-13. F.S.R designed the AFM experiments and statistical analysis in Figures 1B-D, 2B-C and S3-S4. F.S.R. and UC.

bioRxiv preprint doi: https://doi.org/10.1101/2021.02.15.431207; this version posted February 16, 2021. The copyright holder for this preprint (which was not certified by peer review) is the author/funder. All rights reserved. No reuse allowed without permission.

performed and analyzed the AFM experiments shown in Figures 1B-D, 2B-C and S3-S4. UC. performed experiments shown in Figures S9 and S13. N.R performed, analyzed and plotted the experiments shown in Figures 4-7 and Figures S8, S10 and S12-13. U.C performed the experiments shown in Figures 1B-D, 2B-C and S3-S4. S.D and A.C prepared and fully characterized the phosphorylated Httex1 proteins used in Figures 6 and 7D. G.D supervised the experiments shown in Figures 1B-D, 2B-C and S3-S4. All authors reviewed and contributed to the writing.

Competing interests statement

Authors declare no competing financial interests in association with this manuscript.

bioRxiv preprint doi: https://doi.org/10.1101/2021.02.15.431207; this version posted February 16, 2021. The copyright holder for this preprint (which was not certified by peer review) is the author/funder. All rights reserved. No reuse allowed without permission.

References

1 Andrew, S. E. *et al.* The relationship between trinucleotide (CAG) repeat length and clinical features of Huntington's disease. *Nature genetics* **4**, 398-403, doi:10.1038/ng0893-398 (1993).

2 MacDonald, M. E. *et al.* A novel gene containing a trinucleotide repeat that is expanded and unstable on Huntington's disease chromosomes. *Cell* **72**, 971-983, doi:10.1016/0092-8674(93)90585-E (1993).

3 Duyao, M. *et al.* Trinucleotide repeat length instability and age of onset in Huntington's disease. *Nature genetics* **4**, 387-392, doi:10.1038/ng0893-387 (1993).

4 Myers, R. H. *et al.* De novo expansion of a (CAG)n repeat in sporadic Huntington's disease. *Nature genetics* **5**, 168-173, doi:10.1038/ng1093-168 (1993).

5 Persichetti, F. *et al.* Normal and expanded Huntington's disease gene alleles produce distinguishable proteins due to translation across the CAG repeat. *Molecular medicine (Cambridge, Mass.)* **1**, 374-383, doi:10.1007/bf03401575 (1995).

6 Hollenbach, B. *et al.* Aggregation of truncated GST--HD exon 1 fusion proteins containing normal range and expanded glutamine repeats. *Philosophical Transactions of the Royal Society B: Biological Sciences* **354**, 991-994, doi:10.1098/rstb.1999.0450 (1999).

7 Ansaloni, A. *et al.* One-pot semisynthesis of exon 1 of the Huntingtin protein: new tools for elucidating the role of posttranslational modifications in the pathogenesis of Huntington's disease. *Angewandte Chemie (International ed. in English)* **53**, 1928-1933, doi:10.1002/anie.201307510 (2014).

8 Barbaro, B. A. *et al.* Comparative study of naturally occurring huntingtin fragments in Drosophila points to exon 1 as the most pathogenic species in Huntington's disease. *Hum Mol Genet* **24**, 913-925, doi:10.1093/hmg/ddu504 (2015).

9 Mangiarini, L. *et al.* Exon I of the HD gene with an expanded CAG repeat is sufficient to cause a progressive neurological phenotype in transgenic mice. *Cell* **87**, 493-506, doi:10.1016/S0092-8674(00)81369-0 (1996).

10 Martindale, D. *et al.* Length of huntingtin and its polyglutamine tract influences localization and frequency of intracellular aggregates. *Nature genetics* **18**, 150-154, doi:10.1038/ng0298-150 (1998).

11 DiFiglia, M. *et al.* Aggregation of huntingtin in neuronal intranuclear inclusions and dystrophic neurites in brain. *Science* **277**, 1990-1993, doi:10.1126/science.277.5334.1990 (1997).

12 Graveland, G. A., Williams, R. S. & DiFiglia, M. Evidence for degenerative and regenerative changes in neostriatal spiny neurons in Huntington's disease. *Science* **227**, 770-773, doi:10.1126/science.3155875 (1985).

13 Gruber, A. *et al.* Molecular and structural architecture of polyQ aggregates in yeast. *Proceedings of the National Academy of Sciences* **115**, 201717978-201717978, doi:10.1073/pnas.1717978115 (2018).

14 Mattis, V. B. *et al.* Induced pluripotent stem cells from patients with huntington's disease show CAG repeat expansion associated phenotypes. *Cell Stem Cell* **11**, 264-278, doi:10.1016/j.stem.2012.04.027 (2012).

15 Goldberg, Y. P. *et al.* Cleavage of huntingtin by apopain, a proapoptotic cysteine protease, is modulated by the polyglutamine tract. *Nature genetics* **13**, 442-449, doi:10.1038/ng0896-442 (1996).

16 Ochaba, J. *et al.* Potential function for the Huntingtin protein as a scaffold for selective autophagy. *Proceedings of the National Academy of Sciences* **111**, 16889-16894, doi:10.1073/pnas.1420103111 (2014).

17 Pircs, K. *et al.* Huntingtin Aggregation Impairs Autophagy, Leading to Argonaute-2 Accumulation and Global MicroRNA Dysregulation. *Cell Rep* **24**, 1397-1406, doi:10.1016/j.celrep.2018.07.017 (2018).

bioRxiv preprint doi: https://doi.org/10.1101/2021.02.15.431207; this version posted February 16, 2021. The copyright holder for this preprint (which was not certified by peer review) is the author/funder. All rights reserved. No reuse allowed without permission.

18 Wold, M. S., Lim, J., Lachance, V., Deng, Z. & Yue, Z. ULK1-mediated phosphorylation of ATG14 promotes autophagy and is impaired in Huntington's disease models. *Molecular neurodegeneration* **11**, 76, doi:10.1186/s13024-016-0141-0 (2016).

19 Zheng, S. *et al.* Deletion of the huntingtin polyglutamine stretch enhances neuronal autophagy and longevity in mice. *PLoS genetics* **6**, e1000838, doi:10.1371/journal.pgen.1000838 (2010).

20 Becher, M. W. *et al.* Intranuclear neuronal inclusions in Huntington's disease and dentatorubral and pallidoluysian atrophy: Correlation between the density of inclusions and IT15 CAG triplet repeat length. *Neurobiology of Disease* **4**, 387-397, doi:10.1006/nbdi.1998.0168 (1998).

21 Li, H., Li, S. H., Johnston, H., Shelbourne, P. F. & Li, X. J. Amino-terminal fragments of mutant huntingtin show selective accumulation in striatal neurons and synaptic toxicity. *Nature genetics* **25**, 385-389, doi:10.1038/78054 (2000).

22 Lunkes, A. & Mandel, J. L. A cellular model that recapitulates major pathogenic steps of Huntington's disease. *Human Molecular Genetics* **7**, 1355-1361, doi:10.1093/hmg/7.9.1355 (1998).

23 Wellington, C. L. *et al.* Inhibiting caspase cleavage of huntingtin reduces toxicity and aggregate formation in neuronal and nonneuronal cells. *The Journal of biological chemistry* **275**, 19831-19838, doi:10.1074/jbc.M001475200 (2000).

24 Cooper, J. K. *et al.* Truncated N-terminal fragments of huntingtin with expanded glutamine repeats form nuclear and cytoplasmic aggregates in cell culture. *Human Molecular Genetics* **7**, 783-790, doi:10.1093/hmg/7.5.783 (1998).

25 Landles, C. *et al.* Proteolysis of mutant huntingtin produces an exon 1 fragment that accumulates as an aggregated protein in neuronal nuclei in huntington disease. *Journal of Biological Chemistry* **285**, 8808-8823, doi:10.1074/jbc.M109.075028 (2010).

26 Lunkes, A. *et al.* Proteases acting on mutant huntingtin generate cleaved products that differentially build up cytoplasmic and nuclear inclusions. *Molecular cell* **10**, 259-269, doi:10.1016/s1097-2765(02)00602-0 (2002).

27 Kim, Y. J. *et al.* Caspase 3-cleaved N-terminal fragments of wild-type and mutant huntingtin are present in normal and Huntington's disease brains, associate with membranes, and undergo calpaindependent proteolysis. *Proceedings of the National Academy of Sciences of the United States of America* **98**, 12784-12789, doi:10.1073/pnas.221451398 (2001).

28 Wellington, C. L. *et al.* Caspase cleavage of mutant huntingtin precedes neurodegeneration in Huntington's disease. *Journal of Cell Biology* **22**, 749-759, doi:10.1038/35096019 (2002).

29 Wellington, C. L. *et al.* Caspase cleavage of gene products associated with triplet expansion disorders generates truncated fragments containing the polyglutamine tract. *Journal of Biological Chemistry* **273**, 9158-9167, doi:10.1074/jbc.273.15.9158 (1998).

30 Sathasivam, K. *et al.* Aberrant splicing of HTT generates the pathogenic exon 1 protein in Huntington disease. *Proceedings of the National Academy of Sciences* **110**, 2366-2370, doi:10.1073/pnas.1221891110 (2013).

31 Neueder, A. *et al.* The pathogenic exon 1 HTT protein is produced by incomplete splicing in Huntington's disease patients. *Scientific Reports* **7**, 1307-1307, doi:10.1038/s41598-017-01510-z (2017).

32 Brignull, H. R., Morley, J. F., Garcia, S. M. & Morimoto, R. I. Modeling polyglutamine pathogenesis in C. elegans. *Methods in enzymology* **412**, 256-282, doi:10.1016/s0076-6879(06)12016-9 (2006).

33 Fischbeck, K. H. Polyglutamine expansion neurodegenerative disease. *Brain Res Bull* **56**, 161-163 (2001).

34 Hoffner, G. & Djian, P. Polyglutamine Aggregation in Huntington Disease: Does Structure Determine Toxicity? *Mol Neurobiol*, doi:10.1007/s12035-014-8932-1 (2014).

35 Nekooki-machida, Y. *et al.* Distinct conformations of in vitro and in vivo amyloids of huntingtin-exon1 show different cytotoxicity. *Proceedings of the National Academy of Sciences* **106**, 9679-9684, doi:10.1073/pnas.0812083106 (2009).

bioRxiv preprint doi: https://doi.org/10.1101/2021.02.15.431207; this version posted February 16, 2021. The copyright holder for this preprint (which was not certified by peer review) is the author/funder. All rights reserved. No reuse allowed without permission.

36 Thakur, A. K., Yang, W. & Wetzel, R. Inhibition of polyglutamine aggregate cytotoxicity by a structure-based elongation inhibitor. *FASEB J* **18**, 923-925, doi:10.1096/fj.03-1238fje (2004).

37 Davies, S. W. *et al.* Formation of Neuronal Intranuclear Inclusions Underlies the Neurological Dysfunction in Mice Transgenic for the HD Mutation. *Cell* **90**, 537-548 (1997).

38 Arndt, J. R., Chaibva, M. & Legleiter, J. The emerging role of the first 17 amino acids of huntingtin in Huntington's disease. *Biomolecular concepts* **6**, 33-46, doi:10.1515/bmc-2015-0001 (2015).

39 Costanzo, M. *et al.* Transfer of polyglutamine aggregates in neuronal cells occurs in tunneling nanotubes. *Journal of Cell Science* **126**, 3678-3685, doi:10.1242/jcs.126086 (2013).

40 Jeon, I. *et al.* Human-to-mouse prion-like propagation of mutant huntingtin protein. *Acta Neuropathol* **132**, 577-592, doi:10.1007/s00401-016-1582-9 (2016).

41 Pecho-Vrieseling, E. *et al.* Transneuronal propagation of mutant huntingtin contributes to non–cell autonomous pathology in neurons. *Nature Neuroscience* **17**, 1064-1072, doi:10.1038/nn.3761 (2014).

42 Babcock, D. T. & Ganetzky, B. Transcellular spreading of huntingtin aggregates in the Drosophila brain. *Proceedings of the National Academy of Sciences* **112**, E5427-E5433, doi:10.1073/pnas.1516217112 (2015).

43 Babcock, D. T. & Ganetzky, B. Non-cell autonomous cell death caused by transmission of Huntingtin aggregates in Drosophila. *Fly (Austin)* **9**, 107-109, doi:10.1080/19336934.2015.1118591 (2015).

44 Melentijevic, I. *et al.* C. elegans neurons jettison protein aggregates and mitochondria under neurotoxic stress. *Nature* **542**, 367-371, doi:10.1038/nature21362 (2017).

45 Masnata, M. & Cicchetti, F. The Evidence for the Spread and Seeding Capacities of the Mutant Huntingtin Protein in in Vitro Systems and Their Therapeutic Implications. *Front Neurosci* **11**, 647, doi:10.3389/fnins.2017.00647 (2017).

46 Chiki, A. *et al.* Mutant Exon1 Huntingtin Aggregation is Regulated by T3 Phosphorylation-Induced Structural Changes and Crosstalk between T3 Phosphorylation and Acetylation at K6. *Angewandte Chemie International Edition*, 1-6, doi:10.1002/anie.201611750 (2017).

47 Crick, S. L., Ruff, K. M., Garai, K., Frieden, C. & Pappu, R. V. Unmasking the roles of N- and C-terminal flanking sequences from exon 1 of huntingtin as modulators of polyglutamine aggregation. *Proceedings of the National Academy of Sciences* **110**, 20075-20080, doi:10.1073/pnas.1320626110 (2013).

48 Jayaraman, M. *et al.* Kinetically competing huntingtin aggregation pathways control amyloid polymorphism and properties. *Biochemistry* **51**, 2706-2716, doi:10.1021/bi3000929 (2012).

49 Thakur, A. K. *et al.* Polyglutamine disruption of the huntingtin exon1 N-terminus triggers a complex aggregation mechanism Ashwani. *Nat Struct Mol Biol* **16**, 380-389, doi:10.1038/nsmb.1570.Polyglutamine (2009).

50 Monsellier, E., Redeker, V., Ruiz-Arlandis, G., Bousset, L. & Melki, R. Molecular interaction between the chaperone Hsc70 and the N-terminal flank of huntingtin exon 1 modulates aggregation. *Journal of Biological Chemistry* **290**, 2560-2576, doi:10.1074/jbc.M114.603332 (2015).

51 Tam, S., Geller, R., Spiess, C. & Frydman, J. The chaperonin TRiC controls polyglutamine aggregation and toxicity through subunit-specific interactions. *Nature Cell Biology* **8**, 1155-1162, doi:10.1038/ncb1477 (2006).

52 Riguet, N. *et al.* Disentangling the sequence, cellular and ultrastructural determinants of Huntingtin nuclear and cytoplasmic inclusion formation. *bioRxiv*, 2020.2007.2029.226977, doi:10.1101/2020.07.29.226977 (2020).

53 Vieweg, S., Ansaloni, A., Wang, Z. M., Warner, J. B. & Lashuel, H. A. An intein-based strategy for the production of tag-free huntingtin exon 1 proteins enables new insights into the polyglutamine dependence of Httex1 aggregation and fibril formation. *Journal of Biological Chemistry* **291**, 12074-12086, doi:10.1074/jbc.M116.713982 (2016).

bioRxiv preprint doi: https://doi.org/10.1101/2021.02.15.431207; this version posted February 16, 2021. The copyright holder for this preprint (which was not certified by peer review) is the author/funder. All rights reserved. No reuse allowed without permission.

54 Ruggeri, F. S., Habchi, J., Cerreta, A. & Dietler, G. AFM-Based Single Molecule Techniques: Unraveling the Amyloid Pathogenic Species. *Curr Pharm Des* **22**, 3950-3970 (2016).

55 Ruggeri, F. S., Šneideris, T., Vendruscolo, M. & Knowles, T. P. J. Atomic force microscopy for single molecule characterisation of protein aggregation. *Arch Biochem Biophys* **664**, 134-148, doi:10.2174/1381612822666160518141911 (2019).

56 Ruggeri, F. S. *et al.* Influence of the β-sheet content on the mechanical properties of aggregates during amyloid fibrillization. *Angewandte Chemie (International ed. in English)* **54**, 2462-2466, doi:10.1002/anie.201409050 (2015).

57 Ruggeri, F. S. *et al.* Identification and nanomechanical characterization of the fundamental single-strand protofilaments of amyloid α-synuclein fibrils. *Proceedings of the National Academy of Sciences of the United States of America* **115**, 7230-7235 (2018).

58 Atwal, R. S. *et al.* Huntingtin has a membrane association signal that can modulate huntingtin aggregation, nuclear entry and toxicity. *Human Molecular Genetics* **16**, 2600-2615, doi:10.1093/hmg/ddm217 (2007).

59 Hegde, R. N. *et al.* TBK1 phosphorylates mutant Huntingtin and suppresses its aggregation and toxicity in Huntington's disease models. *The EMBO journal*, e104671, doi:10.15252/embj.2020104671 (2020).

60 Williamson, T. E., Vitalis, A., Crick, S. L. & Pappu, R. V. Modulation of polyglutamine conformations and dimer formation by the N-terminus of huntingtin. *Journal of molecular biology* **396**, 1295-1309, doi:10.1016/j.jmb.2009.12.017 (2010).

61 Arrasate, M., Mitra, S., Schweitzer, E. S., Segal, M. R. & Finkbeiner, S. Inclusion body formation reduces levels of mutant huntingtin and the risk of neuronal death. *Nature* **431**, 805-810, doi:10.1038/nature02998 (2004).

62 Bäuerlein, F. J. B. *et al.* In Situ Architecture and Cellular Interactions of PolyQ Inclusions. *Cell* **171**, 179-187.e110, doi:10.1016/j.cell.2017.08.009 (2017).

63 Firdaus, W. J. J. *et al.* Huntingtin inclusion bodies are iron-dependent centers of oxidative events. *FEBS Journal*, doi:10.1111/j.1742-4658.2006.05537.x (2006).

64 Iwata, A., Riley, B. E., Johnston, J. A. & Kopito, R. R. HDAC6 and microtubules are required for autophagic degradation of aggregated Huntingtin. *Journal of Biological Chemistry* **280**, 40282-40292, doi:10.1074/jbc.M508786200 (2005).

65 Liu, K. Y. *et al.* Disruption of the nuclear membrane by perinuclear inclusions of mutant huntingtin causes cell-cycle re-entry and striatal cell death in mouse and cell models of Huntington's disease. *Human Molecular Genetics* **24**, 1602-1616, doi:10.1093/hmg/ddu574 (2015).

66 Lu, M. *et al.* Live-cell super-resolution microscopy reveals a primary role for diffusion in polyglutamine-driven aggresome assembly. *JBC*, doi:10.1074/jbc.RA118.003500 (2018).

67 Mantha, N., Das, N. G. & Das, S. K. Recent Trends in Detection of Huntingtin and Preclinical Models of Huntington ' s Disease. *ISRN Molecular Biology* **2014**, doi:10.1155/2014/190976 (2014).

68 Miller, J., Shaby, B. A., Mitra, S., Masliah, E. & Finkbeiner, S. Quantitative Relationships between Huntingtin Levels , Polyglutamine Length , Inclusion Body Formation , and Neuronal Death Provide Novel Insight into Huntington ' s Disease Molecular Pathogenesis. *The Journal of neuroscience : the official journal of the Society for Neuroscience* **30**, 10541-10550, doi:10.1523/JNEUROSCI.0146-10.2010 (2010).

69 Peskett, T. R. *et al.* A Liquid to Solid Phase Transition Underlying Pathological Huntingtin Exon1 Aggregation. *Molecular cell*, 1-14, doi:10.1016/j.molcel.2018.04.007 (2018).

70 Shen, K. *et al.* Control of the structural landscape and neuronal proteotoxicity of mutant Huntingtin by domains flanking the polyQ tract. *eLife* **5**, 1-29, doi:10.7554/eLife.18065 (2016).

71 Rockabrand, E. *et al.* The first 17 amino acids of Huntingtin modulate its sub-cellular localization, aggregation and effects on calcium homeostasis. *Human Molecular Genetics* **16**, 61-77, doi:10.1093/hmg/ddl440 (2007).

bioRxiv preprint doi: https://doi.org/10.1101/2021.02.15.431207; this version posted February 16, 2021. The copyright holder for this preprint (which was not certified by peer review) is the author/funder. All rights reserved. No reuse allowed without permission.

72 Gu, X. *et al.* Serines 13 and 16 Are Critical Determinants of Full-length Human Mutant Huntingtin-Induced Disease Pathogenesis in HD Mice. *Neuron* **64**, 828-840, doi:10.1016/j.neuron.2009.11.020.Serines (2009).

73 Maiuri, T., Woloshansky, T., Xia, J. & Truant, R. The huntingtin N17 domain is a multifunctional CRM1 and ran-dependent nuclear and cilial export signal. *Human Molecular Genetics* **22**, 1383-1394, doi:10.1093/hmg/dds554 (2013).

74 Greiner, E. R. & Yang, X. W. Huntington's disease: Flipping a switch on huntingtin. *Nature chemical biology* **7**, 412-414, doi:10.1038/nchembio.604 (2011).

75 DeGuire, S. M. *et al.* N-terminal Huntingtin (Htt) phosphorylation is a molecular switch regulating Htt aggregation, helical conformation, internalization, and nuclear targeting. *Journal of Biological Chemistry* **293**, 18540-18558, doi:10.1074/jbc.RA118.004621 (2018).

76 Colby, D. W. *et al.* Potent inhibition of huntingtin aggregation and cytotoxicity by a disulfide bond-free single-domain intracellular antibody. *Proceedings of the National Academy of Sciences of the United States of America* **101**, 17616-17621, doi:10.1073/pnas.0408134101 (2004).

77 Dahlgren, P. R. *et al.* Atomic force microscopy analysis of the Huntington protein nanofibril formation. *Nanomedicine: Nanotechnology, Biology, and Medicine* **1**, 52-57, doi:10.1016/j.nano.2004.11.004 (2005).

78 Hoop, C. L. *et al.* Huntingtin exon 1 fibrils feature an interdigitated β-hairpin-based polyglutamine core. *Proceedings of the National Academy of Sciences of the United States of America* **113**, 1546-1551, doi:10.1073/pnas.1521933113 (2016).

79 Dawson, P. E., Muir, T. W., Clark-Lewis, I. & Kent, S. B. Synthesis of proteins by native chemical ligation. *Science* **266**, 776-779, doi:10.1126/science.7973629 (1994).

80 Der-Sarkissian, A., Jao, C. C., Chen, J. & Langen, R. Structural organization of alpha-synuclein fibrils studied by site-directed spin labeling. *The Journal of biological chemistry* **278**, 37530-37535, doi:10.1074/jbc.M305266200 (2003).

81 Ruggeri, F. S. *et al.* Nanoscale studies link amyloid maturity with polyglutamine diseases onset. *Scientific Reports* **6**, 31155-31155, doi:10.1038/srep31155 (2016).

82 Margittai, M. & Langen, R. Fibrils with parallel in-register structure constitute a major class of amyloid fibrils: molecular insights from electron paramagnetic resonance spectroscopy. *Quarterly reviews of biophysics* **41**, 265-297, doi:10.1017/s0033583508004733 (2008).

83 Bugg, C. W., Isas, J. M., Fischer, T., Patterson, P. H. & Langen, R. Structural features and domain organization of huntingtin fibrils. *Journal of Biological Chemistry* **287**, 31739-31746, doi:10.1074/jbc.M112.353839 (2012).

84 Isas, J. M., Langen, R. & Siemer, A. B. Solid-State Nuclear Magnetic Resonance on the Static and Dynamic Domains of Huntingtin Exon-1 Fibrils. *Biochemistry* **54**, 3942-3949, doi:10.1021/acs.biochem.5b00281 (2015).

85 Cicchetti, F. *et al.* Mutant huntingtin is present in neuronal grafts in huntington disease patients. *Annals of Neurology* **76**, 31-42, doi:10.1002/ana.24174 (2014).

86 Masnata, M. *et al.* Demonstration of prion - like properties of mutant huntingtin fibrils in both in vitro and in vivo paradigms. *Acta Neuropathologica*, doi:10.1007/s00401-019-01973-6 (2019).

87 Jaunmuktane, Z. & Brandner, S. Invited Review: The role of prion-like mechanisms in neurodegenerative diseases. *Neuropathol Appl Neurobiol*, doi:10.1111/nan.12592 (2019).

88 Isas, J. M. *et al.* Huntingtin fibrils with different toxicity, structure, and seeding potential can be reversibly interconverted. *bioRxiv*, 703769-703769, doi:10.1101/703769 (2019).

89 Gu, X. *et al.* N17 Modifies Mutant Huntingtin Nuclear Pathogenesis and Severity of Disease in HD BAC Transgenic Mice. *Neuron* **85**, 726-741, doi:10.1016/j.neuron.2015.01.008 (2015).

90 Vonsattel, J.-P. *et al.* Neuropathological Classification of Huntington's Disease. *Journal of Neuropathology and Experimental Neurology* **44**, 559-577, doi:10.1097/00005072-198511000-00003 (1985).

bioRxiv preprint doi: https://doi.org/10.1101/2021.02.15.431207; this version posted February 16, 2021. The copyright holder for this preprint (which was not certified by peer review) is the author/funder. All rights reserved. No reuse allowed without permission.

91 Gutekunst, C. a. *et al.* Nuclear and neuropil aggregates in Huntington's disease: relationship to neuropathology. *The Journal of neuroscience : the official journal of the Society for Neuroscience* **19**, 2522-2534, doi:10.1523/jneurosci.5389-07.2008 (1999).

92 Kuemmerle, S. *et al.* Huntington aggregates may not predict neuronal death in Huntington's disease. *Ann Neurol* **46**, 842-849 (1999).

93 Saudou, F., Finkbeiner, S., Devys, D. & Greenberg, M. E. Huntingtin acts in the nucleus to induce apoptosis but death does not correlate with the formation of intranuclear inclusions. *Cell* **95**, 55-56, doi:10.1016/S0092-8674(00)81782-1 (1998).

94 Slow, E. J. *et al.* Absence of behavioral abnormalities and neurodegeneration in vivo despite widespread neuronal huntingtin inclusions. *Proceedings of the National Academy of Sciences of the United States of America* **102**, 11402-11407, doi:10.1073/pnas.0503634102 (2005).

95 Saudou, F. & Humbert, S. The Biology of Huntingtin. *Neuron* **89**, 910-926, doi:10.1016/j.neuron.2016.02.003 (2016).

96 Schilling, G. *et al.* Intranuclear inclusions and neuritic aggregates in transgenic mice expressing a mutant N-terminal fragment of huntingtin. *Human Molecular Genetics* **8**, 397-407, doi:10.1093/hmg/8.3.397 (1999).

97 Ochaba, J. *et al.* PIAS1 Regulates Mutant Huntingtin Accumulation and Huntington's Disease-Associated Phenotypes In Vivo. *Neuron* **90**, 507-520 (2016).

98 Veldman, M. B. *et al.* The N17 domain mitigates nuclear toxicity in a novel zebrafish Huntington's disease model. *Molecular neurodegeneration* **10**, 67 (2015).

99 Landles, C. *et al.* Subcellular Localization And Formation Of Huntingtin Aggregates Correlates With Symptom Onset And Progression In A Huntington'S Disease Model. *Brain Communications* **2**, doi:10.1093/braincomms/fcaa066 (2020).

100 Burke, K. A., Hensal, K. M., Umbaugh, C. S., Chaibva, M. & Legleiter, J. Huntingtin disrupts lipid bilayers in a polyQ-length dependent manner. *Biochimica et biophysica acta* **1828**, 1953-1961, doi:10.1016/j.bbamem.2013.04.025 (2013).

101 Burke, K. A., Kauffman, K. J., Umbaugh, C. S., Frey, S. L. & Legleiter, J. The interaction of polyglutamine peptides with lipid membranes is regulated by flanking sequences associated with huntingtin. *Journal of Biological Chemistry* **288**, 14993-15005, doi:10.1074/jbc.M112.446237 (2013).

102 Quist, A. *et al.* Amyloid ion channels: a common structural link for protein-misfolding disease. *Proceedings of the National Academy of Sciences of the United States of America* **102**, 10427-10432 (2005).

103 Mahul-Mellier, A. L. *et al.* Fibril growth and seeding capacity play key roles in α-synuclein-mediated apoptotic cell death. *Cell death and differentiation* **22**, 2107-2122, doi:10.1038/cdd.2015.79 (2015).

104 Peters, M. F. *et al.* Nuclear targeting of mutant huntingtin increases toxicity. *Molecular and Cellular Neurosciences* **14**, 121-128, doi:10.1006/mcne.1999.0773 (1999).

105 Digiovanni, L. F., Mocle, A. J., Xia, J. & Truant, R. Huntingtin N17 domain is a reactive oxygen species sensor regulating huntingtin phosphorylation and localization. *Human Molecular Genetics* **25**, 3937-3945, doi:10.1093/hmg/ddw234 (2016).

106 Cariulo, C. *et al.* Phosphorylation of huntingtin at residue T3 is decreased in Huntington's disease and modulates mutant huntingtin protein conformation. *Proceedings of the National Academy of Sciences*, 201705372-201705372, doi:10.1073/pnas.1705372114 (2017).

107 Thompson, L. M. *et al.* IKK phosphorylates Huntingtin and targets it for degradation by the proteasome and lysosome. *Journal of Cell Biology* **187**, 1083-1099, doi:10.1083/jcb.200909067 (2009).

108 Chiki, A. *et al.* Site-specific phosphorylation of Huntingtin exon 1 recombinant proteins enabled by the discovery of novel kinases. *Chembiochem : a European journal of chemical biology*, doi:10.1002/cbic.202000508 (2020).

bioRxiv preprint doi: https://doi.org/10.1101/2021.02.15.431207; this version posted February 16, 2021. The copyright holder for this preprint (which was not certified by peer review) is the author/funder. All rights reserved. No reuse allowed without permission.

109 O'Nuallain, B. *et al.* Kinetics and thermodynamics of amyloid assembly using a high-performance liquid chromatography-based sedimentation assay. *Methods in enzymology* **413**, 34-74, doi:10.1016/s0076-6879(06)13003-7 (2006).

110 Chen, S., Berthelier, V., Yang, W. & Wetzel, R. Polyglutamine aggregation behavior in vitro supports a recruitment mechanism of cytotoxicity. *Journal of molecular biology* **311**, 173-182, doi:10.1006/jmbi.2001.4850 (2001).

111 Rueden, C. T. *et al.* ImageJ2: ImageJ for the next generation of scientific image data. *BMC Bioinformatics* **18**, 529 (2017).

112 Adrian, M., Dubochet, J., Lepault, J. & McDowall, A. W. Cryo-electron microscopy of viruses. *Nature* **308**, 32-36, doi:10.1038/308032a0 (1984).

113 Dubochet, J. *et al.* Cryo-electron microscopy of vitrified specimens. *Quarterly reviews of biophysics* **21**, 129-228, doi:10.1017/s0033583500004297 (1988).

114 Laemmli, U. K. Cleavage of structural proteins during the assembly of the head of bacteriophage T4. *Nature* **227**, 680-685, doi:10.1038/227680a0 (1970).

115 Steiner, P. *et al.* Modulation of receptor cycling by neuron-enriched endosomal protein of 21 kD. *Journal of Cell Biology* **157**, 1197-1209, doi:10.1083/jcb.200202022 (2002).

116 Wigler, M. *et al.* Transfer of purified herpes virus thymidine kinase gene to cultured mouse cells. *Cell* **11**, 223-232, doi:10.1016/0092-8674(77)90333-6 (1977).

117 Mahul-Mellier, A.-L. *et al.* The making of a Lewy body: the role of α-synuclein post-fibrillization modifications in regulating the formation and the maturation of pathological inclusions. *BiorXv* (2018).

118 Mahul-Mellier, A.-L. *et al.* The process of Lewy body formation, rather than simply alpha-synuclein fibrillization, is the major driver of neurodegeneration. *Proceedings of the National Academy of Sciences*, doi:10.1073/1913904117 (2020).

119 Gavrieli, Y., Sherman, Y. & Ben-Sasson, S. A. Identification of programmed cell death in situ via specific labeling of nuclear DNA fragmentation. *The Journal of cell biology* **119**, 493-501 (1992).

bioRxiv preprint doi: https://doi.org/10.1101/2021.02.15.431207; this version posted February 16, 2021. The copyright holder for this preprint (which was not certified by peer review) is the author/funder. All rights reserved. No reuse allowed without permission.

Figure Legends

Figure 1. Aggregation properties of Httex1 and Nt17-truncated Httex1.

A. Aggregation propensity of Httex1 and ΔNt17-Httex1 proteins (6Q–42Q) determined at 7–9 µM for unexpanded Httex1 and ΔNt17-Httex1 (6Q–28Q) proteins, 8 µM for ΔNt17-Httex1-36Q/42Q and 4 µM for Httex1-36/42Q by sedimentation assay. All data (n = 3) was normalized to t_{0h} and are represented as mean ± S.D. **B.** AFM-imaging of Httex1 and ΔNt17-Httex1 aggregates (6Q, 14Q, 22Q, 28Q, 36Q, and 42Q) at 37°C after 72 h for the 6Q–24Q and 5 h for the 36Q/42Q. Scale bars = 0.5µm.

Figure 2. Aggregate morphology of Httex1 and Nt17-truncated Httex1 fibrils.

A-B. Fibril morphology of Httex1 and ΔNt17-Httex1 proteins (28Q, 36Q, 42Q) assessed by TEM (**A**) or AFM (**B**) after 72 h or 168 h at 37°C, respectively. **C.** Quantification of the fibril width by high-resolution AFM. **A.** Scale bars = 200 nm; **B.** Scale bars = 0.2 µm.

Figure 3. Comparison of the *in vitro* aggregation properties of Httex1, ΔNt17-Httex1, and M8P-Httex1 (43Q).

A. The purities of Httex1, ΔNt17-Httex1, and M8P-Httex1 (43Q) were analyzed by Western blotting (WB) using primary mouse anti-Htt (amino acids 1–82, MAB5492). Note that Httex1 proteins lacking the Nt17 domain have a low binding capacity to SDS and show minor migration on SDS gels. **B.** Analysis of the native conformation of Httex1 43Q, ΔNt17-Httex1 43Q, and M8P-Httex1 43Q proteins using a native gel in combination with WB using primary mouse anti-Htt (amino acids 1–82, MAB5492). Httex1 43Q and M8P 43Q form several conformations (smear), whereby M8P-Httex1 43Q has one major conformation (white star), and Httex1 43Q has two major conformations (white dash). ΔNt17-Httex1 43Q shows two distinct conformations (white arrowheads). **C.** Aggregation propensity of Httex1 43Q, ΔNt17-Httex1 43Q and M8P-Httex1 43Q proteins at 3 µM determined by sedimentation assay. All data (n = 4) were normalized to t_{0h} and are represented as mean ± S.D. **D.** Representative images of Httex1 43Q, ΔNt17-Httex1 43Q and M8P-Httex1 43Q fibrils acquired by cryo-EM. Scale bars

bioRxiv preprint doi: https://doi.org/10.1101/2021.02.15.431207; this version posted February 16, 2021. The copyright holder for this preprint (which was not certified by peer review) is the author/funder. All rights reserved. No reuse allowed without permission.

= 100 nm. **E.** Quantification of fibril lengths and fibril widths based on cryo-EM images using ImageJ.

Figure 4. The helical conformation of the N17 domain is a key determinant of Httex1 aggregation and subcellular localization in HEK 293 cells.

A. Representative confocal images of HEK 293 cells overexpressing (for 48 h) the Httex1 constructs (Httex1, ΔNt17-Httex1 or M8P-Httex1) carrying 39Q (**a-f**) or 72Q (**g-l**) either tag-free (**a-c; g-i**) or fused to the GFP tag (**d-f; j-l**). The insets depict higher magnification of transfected HEK 293 cells with inclusions. Representative confocal images from HEK 293 cells transfected with an empty vector, eGFP, and Httex1 16Q constructs are displayed in **Figure S7B**. Forty-eight hours after transfections, Httex1 expression (grey) was detected using a specific primary antibody against the N-terminal part of Htt (amino acids 1–82, MAB5492). Nuclei were stained with DAPI (blue), and the edge of the cells was detected using the Phalloidin-Atto^{549} toxin (red) that specifically binds to F-actin. Scale bar = 20 µm and 5 µm for the inset. A minimum of three images for each independent experiment was acquired for each condition. Each experiment was performed three times. Forty-eight hours after the overexpression of the Httex1 constructs in HEK 293 cells, the percentage of cells containing Httex1 inclusions (**B**), their nuclear and cytosolic distribution (**C**), and their mean size (**D**) were quantified. The graphs represent the mean ± SD of a minimum of three independent experiments. In each experiment, approximately 100 cells for each condition were quantified. $p < 0.05$ = *, $p < 0.0005$ = ***, (ANOVA followed by Tukey-HSD *post hoc* analysis non-modified vs. ΔNt17 or M8P of each condition); $p < 0.001$ = ##, (ANOVA followed by Tukey-HSD *post hoc* analysis, Httex1 39Q vs. Httex1 72Q; $p < 0.05$= $, (ANOVA followed by Tukey-HSD *post hoc* analysis, ΔNt17 39Q-GFP vs. ΔNt17 72Q-GFP).

Figure 5. Httex1 fibrils subcellular localization is strongly dependent on both the sequence and helical conformation of the Nt17 domain.

bioRxiv preprint doi: https://doi.org/10.1101/2021.02.15.431207; this version posted February 16, 2021. The copyright holder for this preprint (which was not certified by peer review) is the author/funder. All rights reserved. No reuse allowed without permission.

A. Confocal images of primary striatal neurons plated on coverslips and treated with Tris buffer (negative control), 0.5 µM of fibrillar (F) Httex1 43Q (WT 43Q F), ΔNt17-Httex1 43Q (ΔN17 43Q F) or M8P-Httex1 43Q (M8P 43Q F) for 1, 3, and 6 days. Neuronal cells were immunostained against MAP2, a specific neuronal marker (green) or against Htt (amino acids 1–82, MAB5492) (red). The nucleus was counterstained with DAPI (blue). Ortho= orthogonal projection. Scale bars = 5 µm. **B.** Distance map of Httex1 PFFs species. The mean distance of the different PFFs species from the edge of the cell was measured from 8 h to 6 days post-treatment. **C.** The subcellular localization of Httex1 PFFs was assessed at the ultrastructural level by correlative light electron microscopy. Fibrillar Httex1 43Q (0.5 µM) was added to primary striatal neurons for 3 days. Neurons plated on dishes with alpha-numerical marked grids were fixed, imaged by confocal microscopy after immunostaining was performed using antibodies specific for MAP2 and for Htt (amino acids 1–82, MAB5492) (inset **b**, scale bar = 5 µm). The selected neuron (**a**) was embedded and cut by ultramicrotome. Serial sections were examined by TEM (**c** and **Figure S10**). Httex1 43Q PFFs (black arrows) mostly accumulate at the outer side of the plasma membrane (highlighted in orange). Few Httex1 43Q PFFs (red star) were detected in endocytic vesicles (highlighted in green). Scales bars = 5 µm (**a**) and 1 µm (**b**).

D. Distribution of the Httex1 PFFs species by compartment (cytosol vs. nucleus) from 8 h to 6 days post-treatment, quantification by the mean intensity. **E.** Ratio of the nuclear and cytosolic distribution of Httex1 PFFs species from 8 h to 6 days post-treatment.

The graphs represent the mean ± SD of a minimum of three independent experiments. In each experiment, five neurons for each condition were quantified. $p < 0.05$ = *, $p < 0.0005$ = ***, (ANOVA followed by Tukey-HSD *post hoc* analysis Tris vs. PFFs species); $p < 0.0005$ = ###, (ANOVA followed by Tukey-HSD *post hoc* analysis, Httex1 PFFs vs. ΔN17- or M8P-Httex1 43Q PFFs).

Figure 6. Phosphorylation of T3, S13, and/or S16 residues promotes the nuclear relocalization of Httex1 monomers after their uptake into primary striatal neurons.

bioRxiv preprint doi: https://doi.org/10.1101/2021.02.15.431207; this version posted February 16, 2021. The copyright holder for this preprint (which was not certified by peer review) is the author/funder. All rights reserved. No reuse allowed without permission.

A. Confocal images of primary striatal neurons plated on coverslips and treated with Tris buffer (negative control), 0.5 µM of pT3 M 23Q, pS13/pS16 M 23Q, or pT3/S13/S16 M 23Q for 1, 3, and 6 days. Neuronal cells were immunostained against MAP2, a specific neuronal marker (green), or Htt (amino acids 1–82, MAB5492) (red). The nucleus was counterstained with DAPI (blue). Scale bar = 20 µm (low magnification) or 5 µm (high magnification and orthogonal section).

B. Nuclear and cytosolic distribution of Httex1 monomeric species (Httex1 23Q, ∆Nt17-Httex1 23Q, or M8P-Httex1 23Q) (nuclear/cytosolic ratio) from 8 h to 6 days post-treatment.

C. Distribution of the Httex1 monomeric species (Httex1 23Q, ∆Nt17-Httex1 23Q, or M8P-Httex1 23Q) by compartment (cytosol vs. nucleus) from 8 h to 6 days post-treatment, quantification by the mean intensity. The graphs represent the mean ± SD of three independent experiments (in each experiment, five neurons for each condition were analyzed). $p < 0.05$ = *, $p < 0.005$ = **, $p < 0.0005$ =* **, (ANOVA followed by Tukey-HSD *post hoc* analysis, Tris vs. monomer species at days 1, 3, and 6 or 23Q vs. monomer species at days 1, 3, and 6 for panel D).

Figure 7. The Nt17 domain and the polyQ length mediate Httex1 toxicity in HEK 293 cells and primary striatal neurons

A-B. Cell death level was assessed in HEK 293 cells transfected for 72 h (**Figure S12**) and 96 h with Httex1 constructs (Httex1, ∆Nt17-Httex1, or M8P-Httex1) carrying 16Q, 39Q, or 72Q either tag-free or fused to the GFP tag. **A.** Loss of cell plasma membrane integrity was assessed using the Sytox blue assay. For each independent experiment, triplicate wells were measured per condition. **B.** Apoptotic activation was assessed using Caspase 3. For each independent experiment, triplicate wells were measured per condition. **A-B.** The graphs represent the mean ± SD of three independent experiments. For each independent experiment, triplicate wells were measured per condition. $p < 0.05$ = * (ANOVA followed by Tukey-HSD *post hoc* analysis, empty vector vs. tag-free Httex1 constructs or GFP vs. GFP-

bioRxiv preprint doi: https://doi.org/10.1101/2021.02.15.431207; this version posted February 16, 2021. The copyright holder for this preprint (which was not certified by peer review) is the author/funder. All rights reserved. No reuse allowed without permission.

tagged Httex1 constructs); $p < 0.05$ = # (ANOVA followed by Tukey-HSD *post hoc* analysis, Httex1-39Q vs. Httex1-72Q).

C-G. Cell death level was assessed in the primary striatal neurons treated for 6 days with 0.5 µM of Httex1 monomeric species (Httex1 23Q, ΔNt17-Httex1 23Q, or M8P-Httex 23Q) (**C**) or [Httex1 23Q, pT3-Httex1 23Q (pT3) or pS13/pS16-httex1 23Q (pS13/pS16) and pT3/pS13/pS16-httex1 23Q (pS13/pS16)] (**D**) or with increasing concentrations (0.5, 1, or 2 µM) of Httex1 23Q or 43Q PFFs (**E**) or Httex1 43Q, ΔNt17-Httex1 43Q or M8P-Httex 43Q (**F**) or with 2 µM Httex1 43Q, ΔNt17-Httex1 43Q, or M8P-Httex 43Q (**G**). **C-F.** Loss of cell plasma membrane integrity was assessed using the Sytox Green assay. For each independent experiment, triplicate wells were measured per condition **G.** Activation of the apoptotic pathways was confirmed by the TUNEL (Terminal dUTP Nick End-Labeling) assay. The neuronal population was positively stained for a specific neuronal marker (NeuN), and the nucleus was counterstained using DAPI (**Figure S12G**). The percentage of apoptotic neurons was quantified as follows: [(TUNEL-positive and NeuN-positive cells)/total NeuN-positive cells]. For each independent experiment, three fields of view, with an average of 150 cells/field, were quantified per condition.

F-G. The graphs represent the mean ± SD of a minimum of three independent experiments. $p < 0.05$ = *, $p < 0.005$ = **, $p < 0.0005$ = 0.0005 (ANOVA followed by Tukey-HSD *post hoc* analysis, Tris vs. Httex1 species). $p < 0.05$ = #, $p < 0.005$ = ##, (ANOVA followed by Tukey-HSD *post hoc* analysis, Httex1 43Q PFFs vs. ΔNt17- or M8P-Httex 43Q PFFs). $p < 0.005$ = $$, (ANOVA followed by Tukey-HSD *post hoc* analysis, Httex1 43Q PFFs vs. ΔNt17- or M8P-Httex 43Q PFFs).

Figure 8. The role of the Nt17 domain in regulating the quaternary packing of Httex1 into fibrils and the internalization of Httex1 fibrils.

A. Illustration of the aggregation pathway of Httex1. Based on the synergistic effect of the Nt17 and polyQ domains on Httex1 aggregation and aggregate structure, we propose a model where the Nt17 domain induces an amyloidogenic polyQ conformation, which facilitates the

bioRxiv preprint doi: https://doi.org/10.1101/2021.02.15.431207; this version posted February 16, 2021. The copyright holder for this preprint (which was not certified by peer review) is the author/funder. All rights reserved. No reuse allowed without permission.

oligomerization step of Httex1 aggregation. **B-C.** Model of the arrangement of the β-sheet network in Httex1 fibrils (**B**) and ΔNt17-Httex1 fibrils (**C**). **D.** Schematic depiction of the Nt17-inhibiting effect on the uptake of Httex1 fibrils into primary rat striatal neurons. The Nt17 domain is exposed in Httex1 fibrils and can interact with the plasma membrane, thus interfering with internalization. The deletion of the Nt17 domain or disruption of the Nt17 helix by the M8P mutation abolishes the Nt17 membrane binding capacity and allows for rapid fibril uptake into neurons.

Figure 1

A

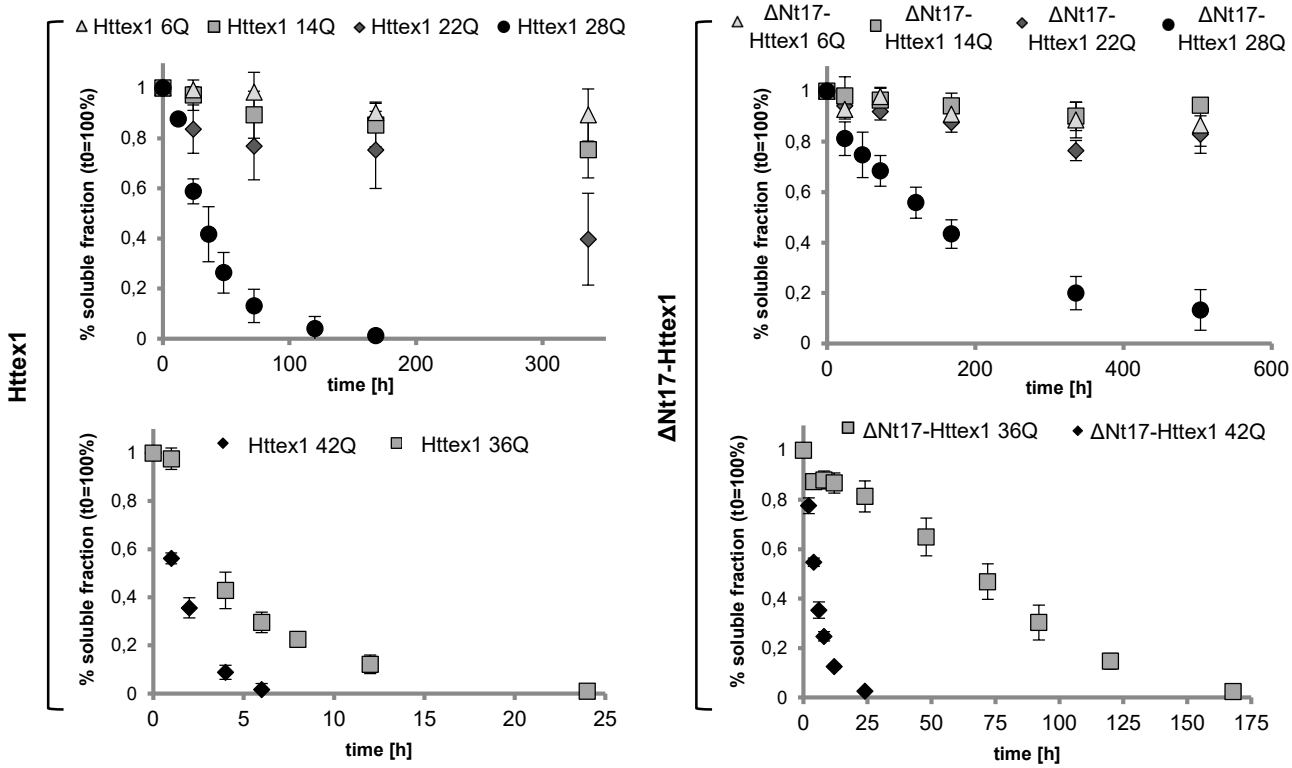
Htttex1
Htttex1 6Q
Htttex1 14Q
Htttex1 22Q
Htttex1 28Q
% soluble fraction (t0=100%)
time [h]
Htttex1 42Q
Htttex1 36Q
ΔNt17-Htttex1
ΔNt17-Htttex1 6Q
ΔNt17-Htttex1 14Q
ΔNt17-Htttex1 22Q
ΔNt17-Htttex1 28Q
ΔNt17-Htttex1 36Q
ΔNt17-Htttex1 42Q

B

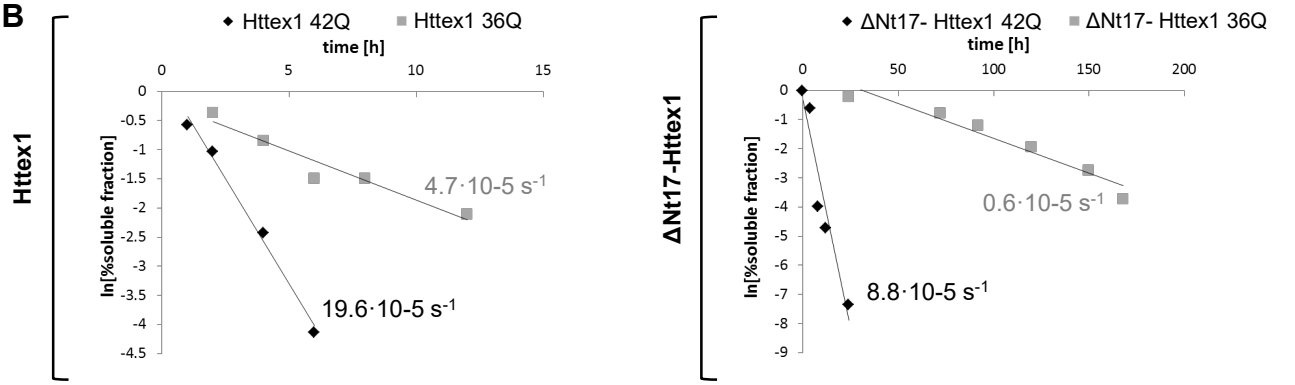
Htttex1
Htttex1 42Q
Htttex1 36Q
time [h]
ln[%soluble fraction]
4.7·10-5 s-1
19.6·10-5 s-1
ΔNt17-Htttex1
ΔNt17- Htttex1 42Q
ΔNt17- Htttex1 36Q
0.6·10-5 s-1
8.8·10-5 s-1

C

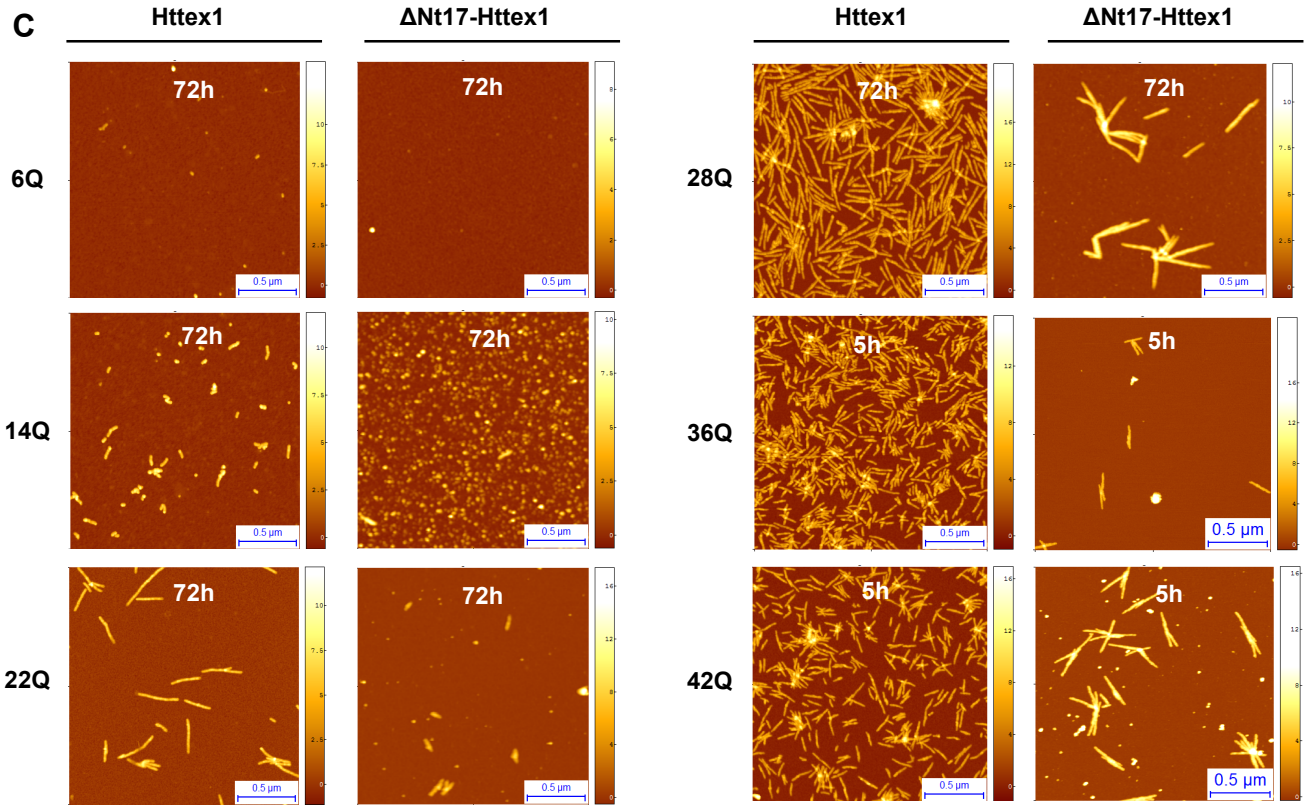
Htttex1
ΔNt17-Htttex1
6Q
14Q
22Q
28Q
36Q
42Q
72h
5h
0.5 µm

Figure 2

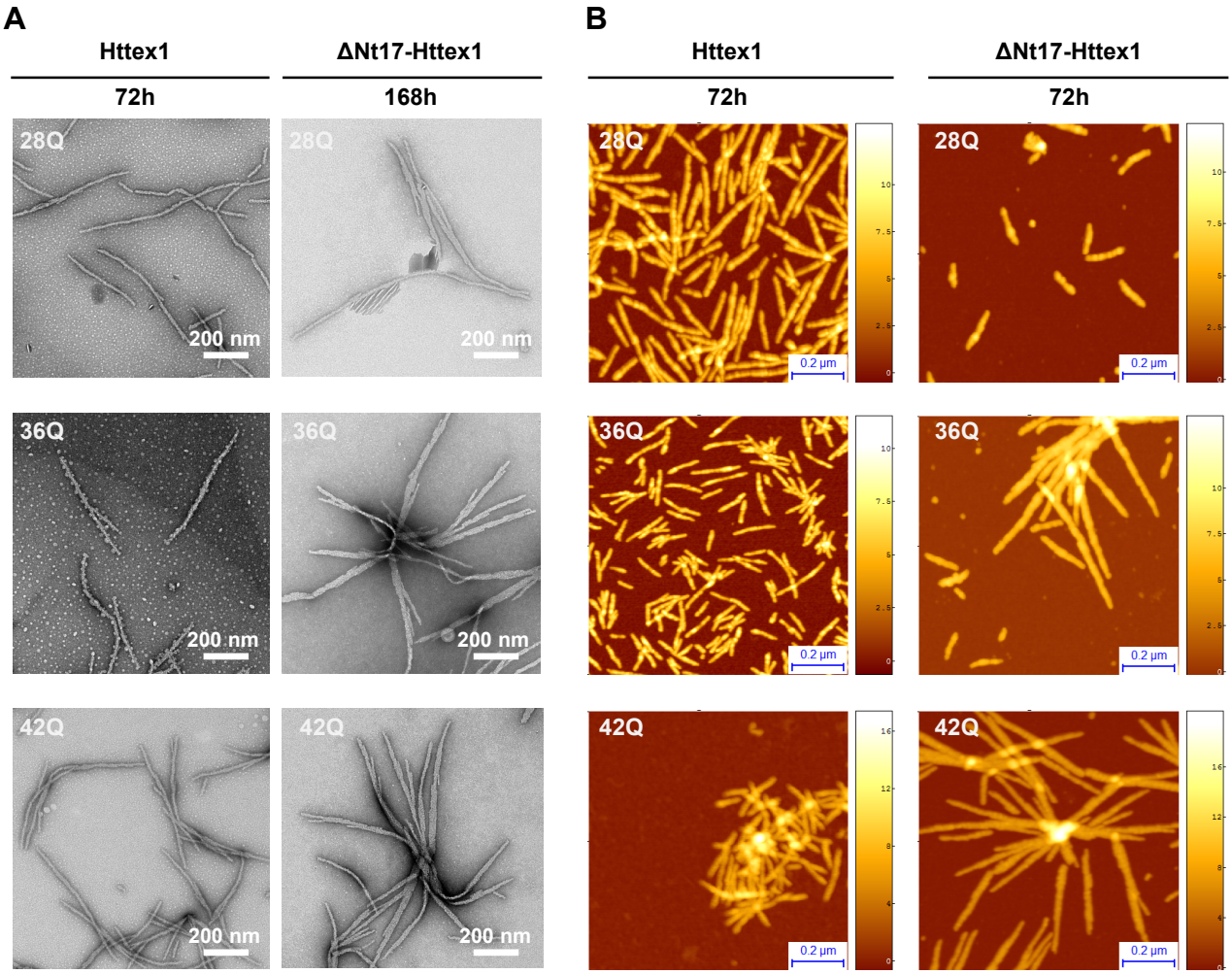
A
Httex1
ΔNt17-Httex1
72h
168h
28Q
36Q
42Q
200 nm
B
Httex1
ΔNt17-Httex1
72h
72h
0.2 µm

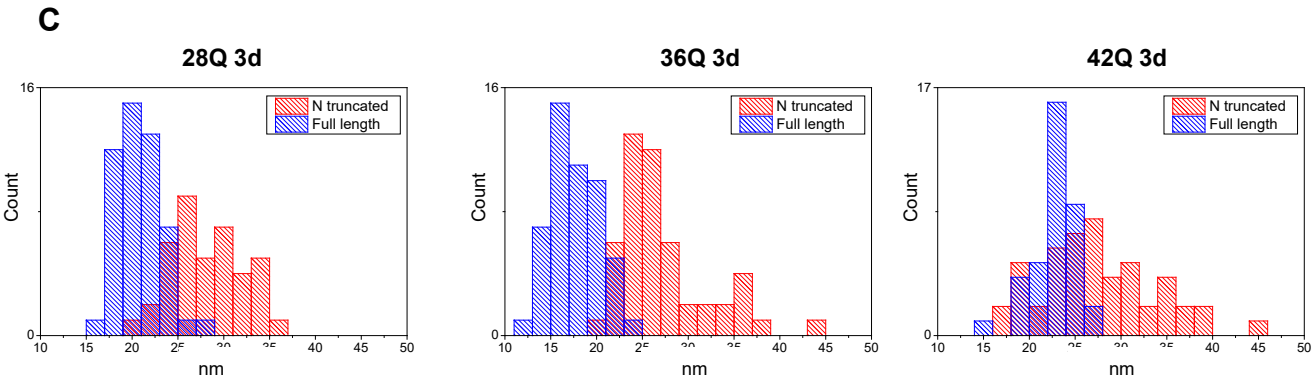
C
28Q 3d
36Q 3d
42Q 3d
N truncated
Full length
Count
nm

Figure 3

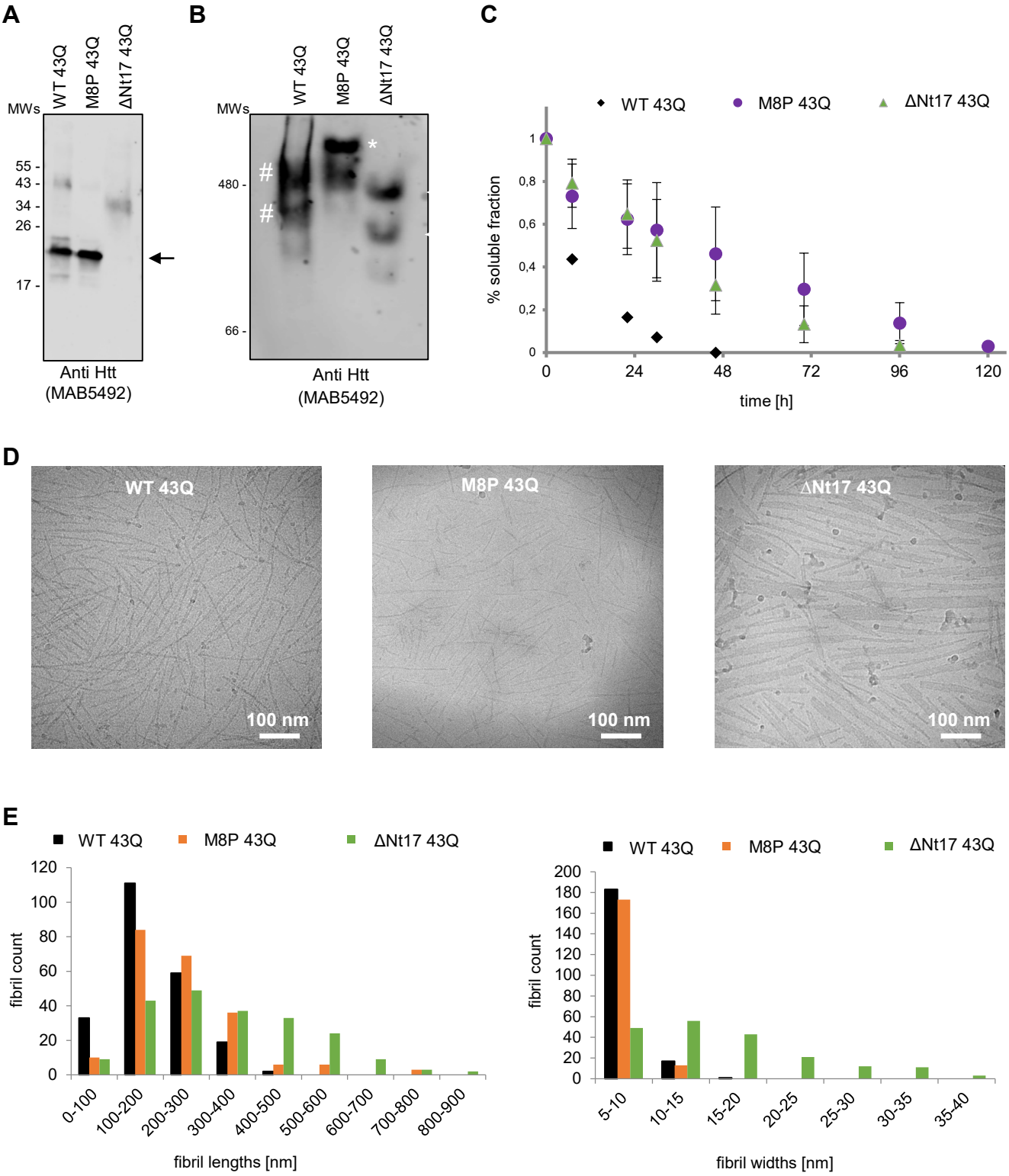
A
WT 43Q
M8P 43Q
ΔNt17 43Q
MWs
55 -
43 -
34 -
26 -
17 -
Anti Htt
(MAB5492)
B
WT 43Q
M8P 43Q
ΔNt17 43Q
MWs
480 -
66 -
#
#
*
Anti Htt
(MAB5492)
C
WT 43Q
M8P 43Q
ΔNt17 43Q
% soluble fraction
1
0,8
0,6
0,4
0,2
0
0
24
48
72
96
120
time [h]
D
WT 43Q
100 nm
M8P 43Q
100 nm
ΔNt17 43Q
100 nm
E
WT 43Q
M8P 43Q
ΔNt17 43Q
fibril count
120
100
80
60
40
20
0
0-100
100-200
200-300
300-400
400-500
500-600
600-700
700-800
800-900
fibril lengths [nm]
WT 43Q
M8P 43Q
ΔNt17 43Q
fibril count
200
180
160
140
120
100
80
60
40
20
0
5-10
10-15
15-20
20-25
25-30
30-35
35-40
fibril widths [nm]

Figure 4

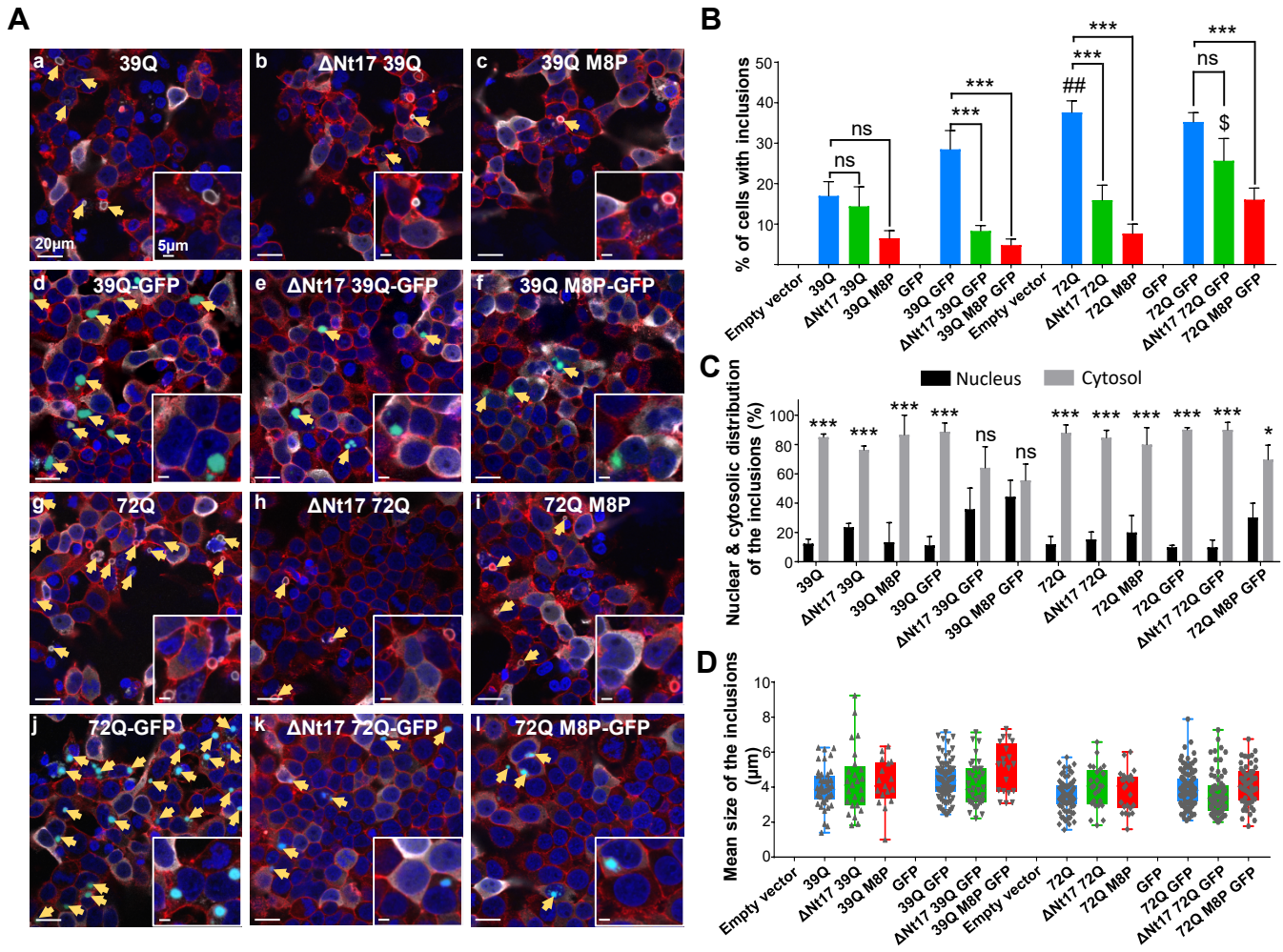
A
a 39Q
b ΔNt17 39Q
c 39Q M8P
20µm
5µm
d 39Q-GFP
e ΔNt17 39Q-GFP
f 39Q M8P-GFP
g 72Q
h ΔNt17 72Q
i 72Q M8P
j 72Q-GFP
k ΔNt17 72Q-GFP
l 72Q M8P-GFP
B
% of cells with inclusions
Empty vector
39Q
ΔNt17 39Q
39Q M8P
GFP
39Q GFP
ΔNt17 39Q GFP
39Q M8P GFP
72Q
ΔNt17 72Q
72Q M8P
72Q GFP
ΔNt17 72Q GFP
72Q M8P GFP
ns
***
##
$
C
Nucleus
Cytosol
Nuclear & cytosolic distribution of the inclusions (%)
D
Mean size of the inclusions (µm)

Figure 5

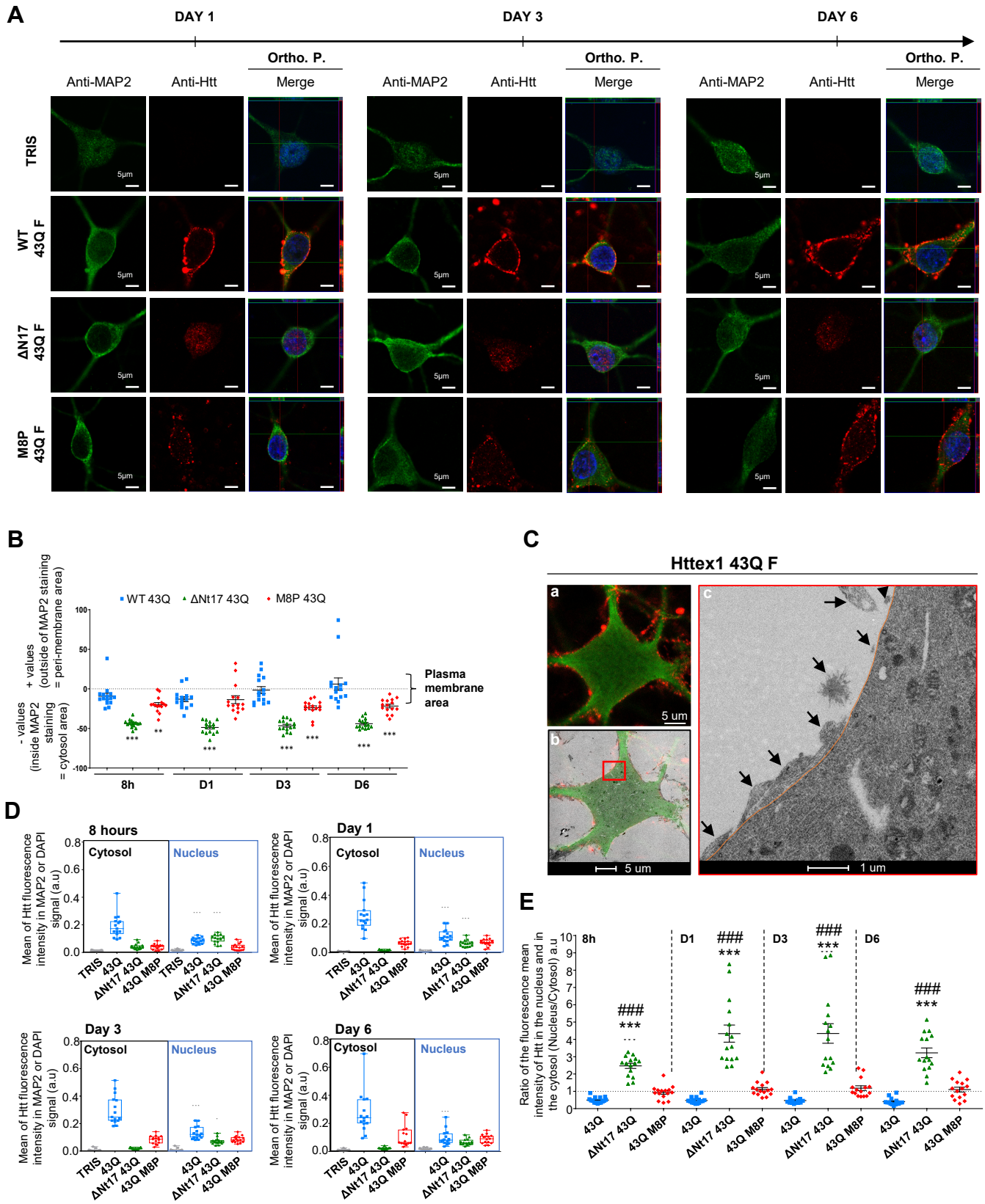
A
DAY 1
DAY 3
DAY 6
Ortho. P.
Anti-MAP2
Anti-Htt
Merge
TRIS
WT 43Q F
ΔN17 43Q F
M8P 43Q F
5µm
B
WT 43Q
ΔNt17 43Q
M8P 43Q
+ values (outside of MAP2 staining = peri-membrane area)
- values (inside MAP2 staining = cytosol area)
Plasma membrane area
8h
D1
D3
D6
C
Httex1 43Q F
5 um
1 um
D
8 hours
Day 1
Day 3
Day 6
Cytosol
Nucleus
Mean of Htt fluorescence intensity in MAP2 or DAPI signal (a.u)
TRIS
43Q
ΔNt17 43Q
43Q M8P
E
Ratio of the fluorescence mean intensity of Htt in the nucleus and in the cytosol (Nucleus/Cytosol) a.u

Figure 6

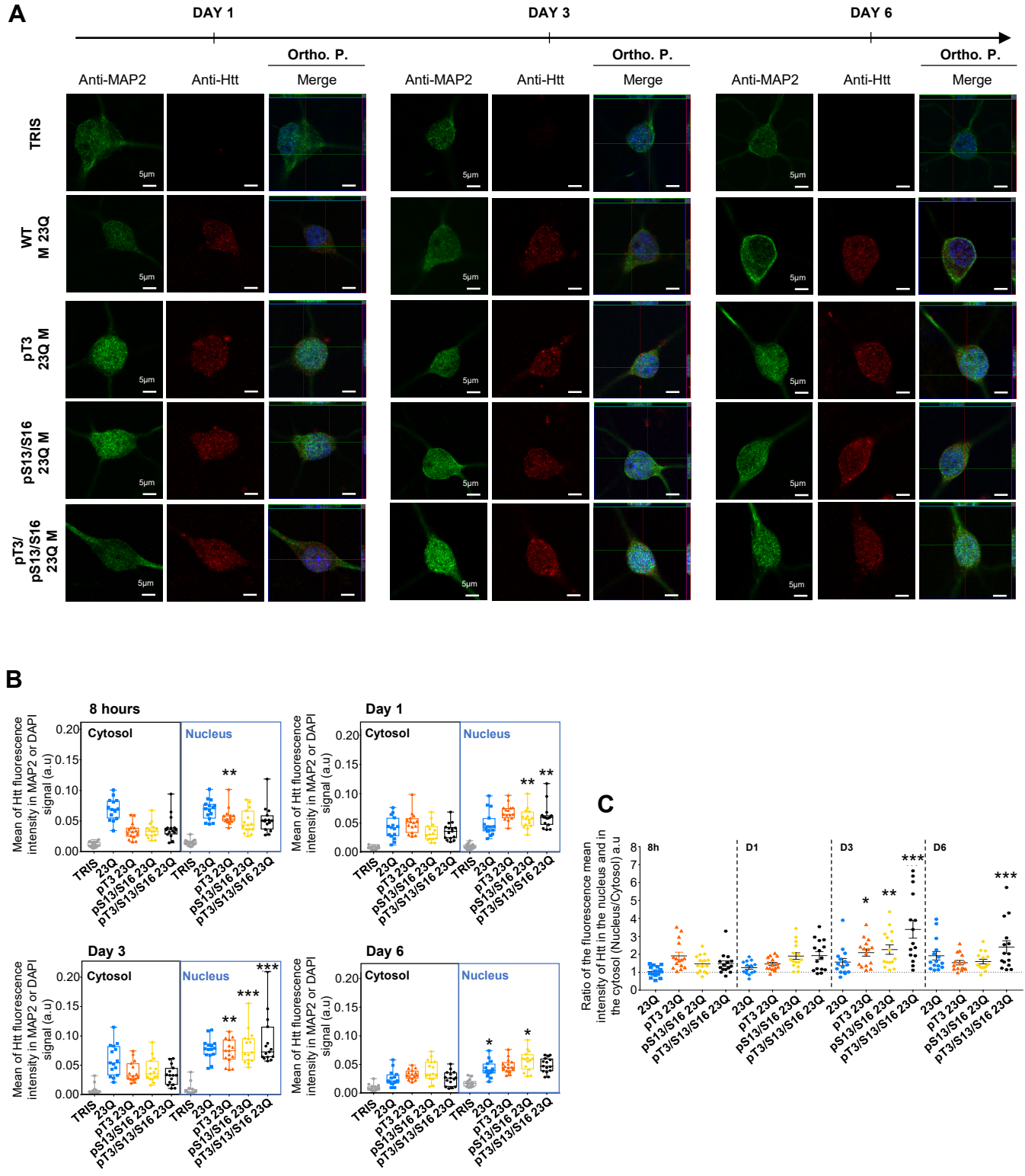
A
DAY 1
DAY 3
DAY 6
Ortho. P.
Anti-MAP2
Anti-Htt
Merge
TRIS
WT M 23Q
pT3 23Q M
pS13/S16 23Q M
pT3/ pS13/S16 23Q M
5µm
B
8 hours
Day 1
Day 3
Day 6
Cytosol
Nucleus
Mean of Htt fluorescence intensity in MAP2 or DAPI signal (a.u)
TRIS
23Q
pT3 23Q
pS13/S16 23Q
pT3/S13/S16 23Q
C
8h
D1
D3
D6
Ratio of the fluorescence mean intensity of Htt in the nucleus and in the cytosol (Nucleus/Cytosol) a.u

Figure 7

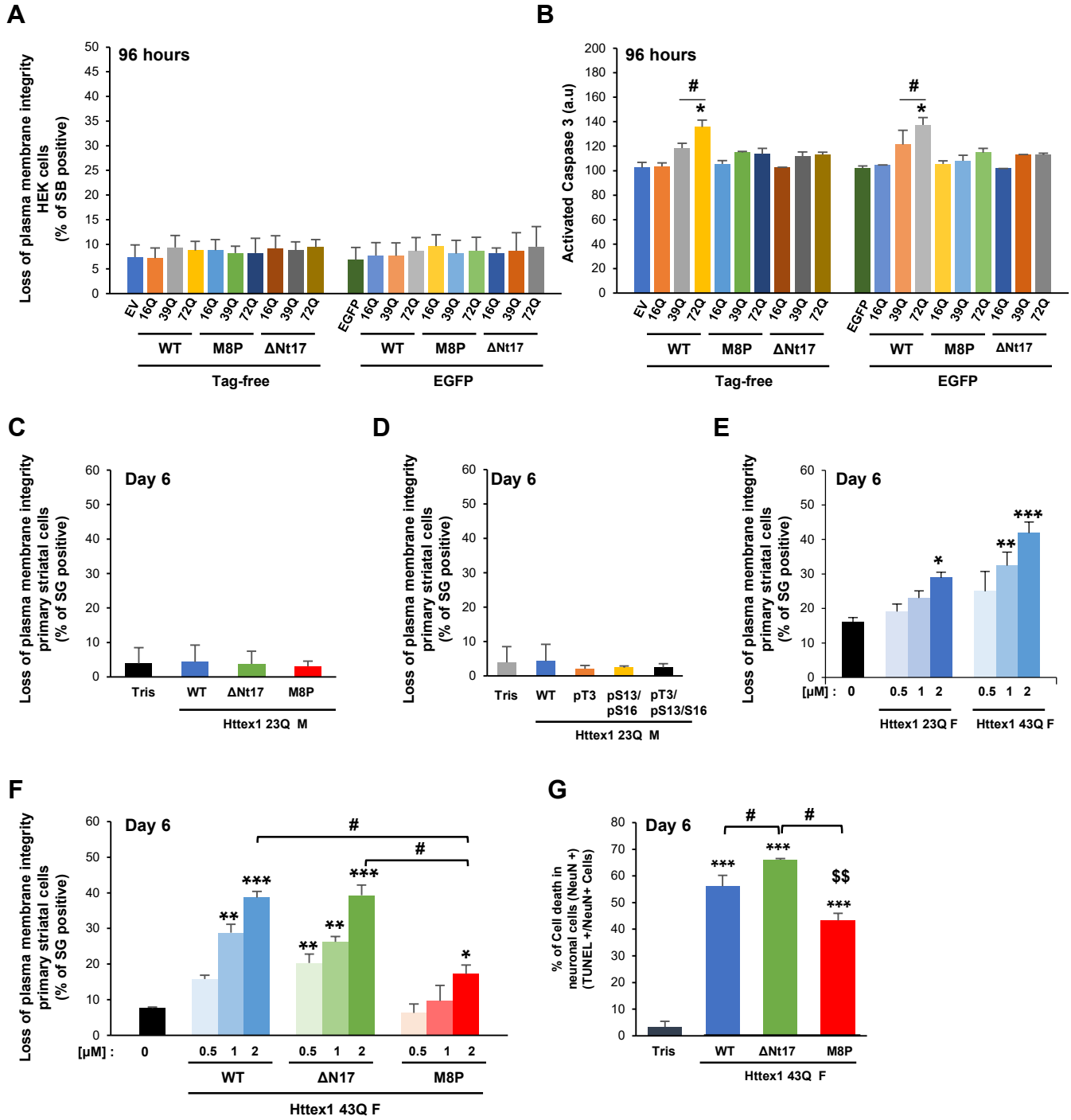
A
96 hours
Loss of plasma membrane integrity HEK cells (% of SB positive)
EV 16Q 39Q 72Q 16Q 39Q 72Q 16Q 39Q 72Q
EGFP 16Q 39Q 72Q 16Q 39Q 72Q 16Q 39Q 72Q
WT M8P ΔNt17
Tag-free
EGFP
B
96 hours
Activated Caspase 3 (a.u)
#
*
Tag-free
EGFP
C
Day 6
Loss of plasma membrane integrity primary striatal cells (% of SG positive)
Tris WT ΔNt17 M8P
Httex1 23Q M
D
Day 6
Tris WT pT3 pS13/ pS16 pT3/ pS13/S16
Httex1 23Q M
E
Day 6
[μM] : 0 0.5 1 2 0.5 1 2
Httex1 23Q F
Httex1 43Q F
F
Day 6
[μM] : 0 0.5 1 2 0.5 1 2 0.5 1 2
WT ΔN17 M8P
Httex1 43Q F
G
Day 6
% of Cell death in neuronal cells (NeuN +) (TUNEL +/NeuN+ Cells)
$$
Tris WT ΔNt17 M8P
Httex1 43Q F

Figure 8

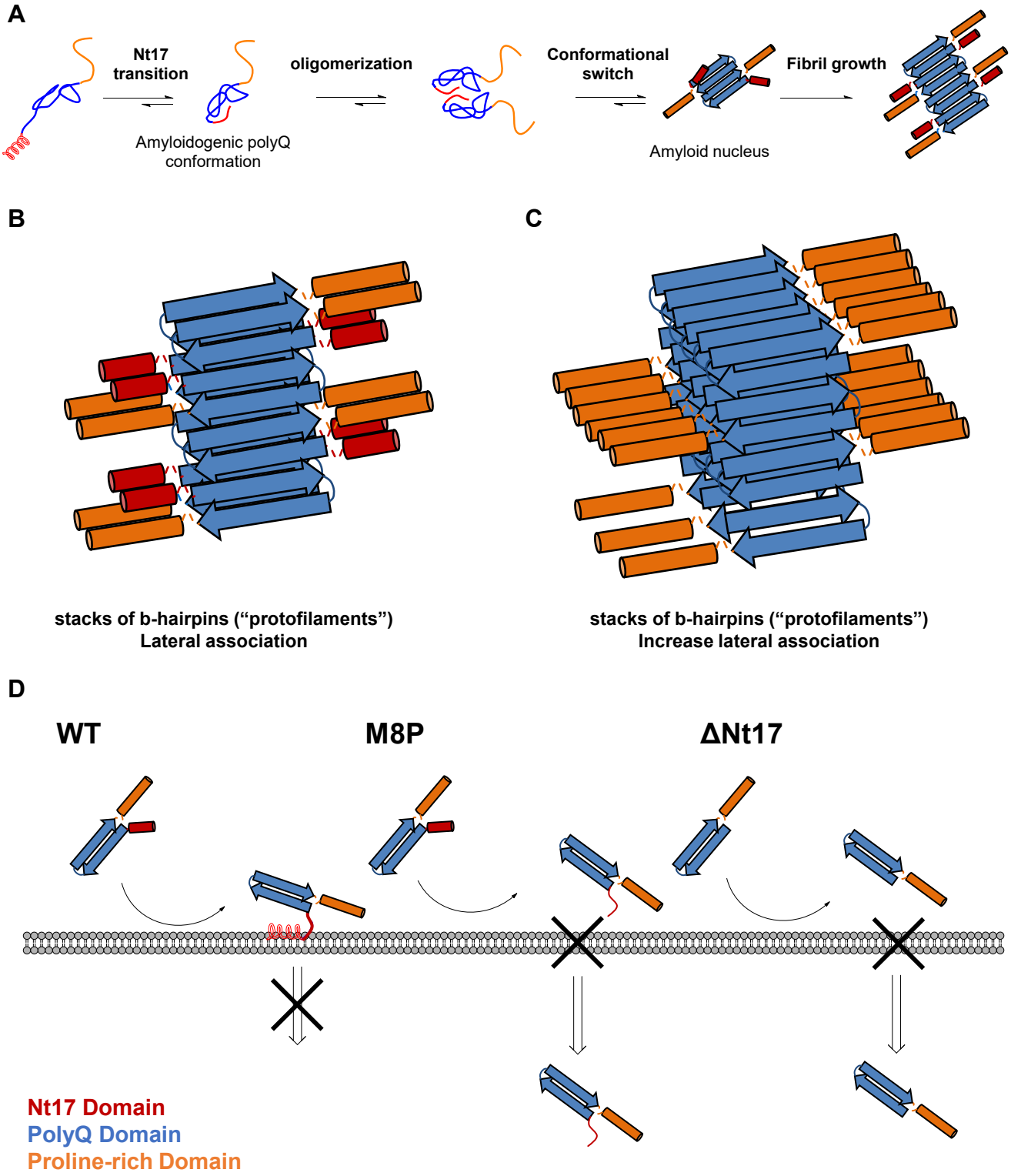
A
Nt17
transition
Amyloidogenic polyQ
conformation
oligomerization
Conformational
switch
Amyloid nucleus
Fibril growth
B
stacks of b-hairpins ("protofilaments")
Lateral association
C
stacks of b-hairpins ("protofilaments")
Increase lateral association
D
WT
M8P
ΔNt17
Nt17 Domain
PolyQ Domain
Proline-rich Domain